Nuclear disruption as a mechanism of the chemotherapeutic drug paclitaxel in interphase

Thomas Hale, Victoria L Hale, Piotr Kolata, Ália dos Santos* & Matteo Allegretti*

*Address correspondence to: Dr Ália dos Santos, adossantos@mrc-lmb.cam.ac.uk; or Dr Matteo Allegretti, matteoall@mrc-lmb.cam.ac.uk; Structural Studies Division, MRC Laboratory of Molecular Biology, Cambridge, UK.

Abstract

Paclitaxel is a microtubule stabilising drug used to treat breast, ovarian, and lung cancers. Its anticancer mechanism is thought to rely on mitotic arrest of fast-dividing cells and subsequent apoptosis following mitotic spindle disruption. However, paclitaxel reduces tumour size even in slow-dividing tumours, indicating an alternative, poorly characterised mechanism in interphase. Understanding paclitaxel's less characterised effects is important for more effective cancer treatments, reducing tumour resistance and drug toxicity in healthy cells.

Here, we found that paclitaxel-induced microtubule reorganisation in interphase also affects the perinuclear distribution of actin and vimentin filaments. The formation of large microtubule-vimentin bundles coincided with nuclear shape deformation, nuclear envelope invaginations, loss of control of nuclear membrane spacing, and changes to nuclear lamina organisation. Concurrently, Lamin A/C protein levels were decreased, and this depended on nuclear-cytoskeletal connectivity through LINC complex component SUN2. Finally, we show that Lamin A/C expression levels, which are often aberrant in cancer cells, are important in determining cell sensitivity to paclitaxel and recovery from treatment. Overall, our data supports nuclear architecture disruption as an additional mechanism for paclitaxel during interphase and independent of mitotic arrest.

Abbreviations

Cryo-FIB, cryo-focused ion beam; cryo-FIB/SEM, cryo-FIB milling with Scanning Electron Microscopy; cryo-ET, electron cryo-tomography; DMEM, Dulbecco's modified Eagle's medium; GIS, gas injection system; hTERT, human telomerase reverse transcriptase; INM, inner nuclear membrane; LINC complex, Linker of Nucleoskeleton and Cytoskeleton complex; Li's ICQ, Li's Intensity Correlation Quotient; MTOC, microtubule organising centre; NE, nuclear envelope; ONM, outer nuclear membrane; SEM, standard error of the mean; STORM, stochastic optical reconstruction microscopy; TBS, Tris-buffered saline.

Introduction

Paclitaxel is a chemotherapeutic drug widely used to treat breast, ovarian and lung cancers[1–3]. It acts by binding stoichiometrically to β-tubulin within microtubules and inducing conformational changes that stabilise interactions between adjacent α/β-tubulin heterodimers[4], preventing microtubule depolymerisation and enhancing bundle formation[5,6]. Previous hypotheses for paclitaxel's anti-cancer mechanism are centred around its suppression of microtubule dynamics in the mitotic spindle, which disrupts chromosome segregation and activates the mitotic checkpoint to result in cell cycle arrest and subsequently apoptosis[7]. However, paclitaxel reduces tumour size even in tumours with low duplication rates and where only a small fraction of cells is proliferative[8–10], suggesting an additional mechanism of action outside of mitosis[11]. This interphase anti-tumour activity of paclitaxel is still poorly understood.

Paclitaxel has been shown to result in microtubule re-organisation around the nucleus during interphase[12,13], alongside deformation of the nucleus and ectopic localisation of nuclear envelope (NE) and lamina proteins in cancer cells[14,15]. This suggests that a potential anti-cancer mechanism of paclitaxel may be via the disruption of nuclear-cytoskeletal coupling, leading to an increased risk of DNA damage and consequent cell death[16–18]. Nuclear-cytoskeletal coupling is mediated by Linker of Nucleoskeleton and Cytoskeleton (LINC) complexes, which consist of a trimer of SUN proteins that span the inner nuclear membrane and interact at the C-terminal end of a periplasmic coiled-coil region with the C-terminus of three KASH protein monomers[19]. KASH proteins traverse the outer nuclear membrane and connect to the cytoskeleton in the cytoplasm at their N-terminus[20], while the N-terminus of SUN proteins connects to the nuclear lamina in the nuceloplasm[21]. Cytoskeletal forces are therefore transmitted to the nuclear lamina and linked chromatin domains via these direct connections, which provide the physical basis for mechanotransduction[22].

In nuclear-cytoskeletal coupling, the nuclear lamina plays an important role in controlling the mechanical response of the nucleus, ensuring it can withstand and react to mechanical forces[23,24]. The nuclear lamina consists of the A-type lamins Lamin A and C, which are splice isoforms of the *LMNA* gene, as well as the B-type lamins Lamin B1 and B2[25]. These are intermediate filament proteins that polymerise to form a filamentous mesh beneath the NE[25]. Aberrations to the nuclear lamina and nuclear morphology are prevalent across many cancer types and are often used as biomarkers in diagnosis[26]. In particular, Lamin A/C expression is frequently altered in cancer cells[27–31], which is thought to play a role in migration and invasion, a hallmark of cancer that leads to metastasis[31]. However, alterations to the nuclear lamina may also make cancer cells particularly sensitive to perturbations to nuclear-cytoskeletal coupling. In

support of this, decreased Lamin A/C expression has been shown to increase sensitivity to paclitaxel in ovarian cancer cells[14].

Here we propose that cancer cells are more vulnerable to paclitaxel outside of mitosis because their aberrant NE and nuclear lamina makes them more susceptible to further nuclear deformations. Supporting this, we observed that paclitaxel reorganises microtubule, actin, and vimentin filaments around the nucleus during interphase in human fibroblasts, which deforms both the overall nuclear shape and NE. The nuclear lamina is also disrupted as it has a patchy appearance upon paclitaxel treatment alongside decreased Lamin A/C levels, and we show that this phenotype occurs via connection to SUN2-containing LINC complexes. Finally, we show that nuclear deformation is dependent upon Lamin A/C expression levels, which also affect overall sensitivity to paclitaxel and, most importantly, recovery from it.

Results

Paclitaxel induces cytoskeletal reorganisation around the nucleus during interphase

To investigate how paclitaxel affects the organisation of microtubules during interphase, human fibroblasts were treated with 5 nM paclitaxel or control media for 16 h. This concentration and timepoint are within the clinically relevant range[32] and align with previous studies[7,14,15]. Cells were analysed by immunofluorescence confocal microscopy for α-tubulin and stained for DNA with Hoechst (Figure 1A). In contrast to control cells where microtubules were dispersed throughout the cytoplasm and emanated from a single microtubule organising centre (MTOC), in paclitaxel-treated cells the microtubules formed dense rings around the nucleus with no single obvious MTOC (Figure 1A).

To determine if these microtubules surrounding the nucleus are bundled, we used 2D stochastic optical reconstruction microscopy (STORM), which allowed microtubule bundles to be resolved and characterised morphologically (Figure 1B). Quantitative HDBSCAN clustering of STORM data revealed an increase of 42% in the microtubule bundle diameter in the presence of paclitaxel compared to untreated cells (Figure 1C).

Since there is extensive crosstalk between microtubule, actin, and intermediate filaments[33,34], we next tested how the organisation of actin and vimentin is affected by paclitaxel treatment (Figure 1D and E). As expected, actin filaments were distributed throughout the cortex in control cells, but in the presence of paclitaxel, perinuclear actin was instead condensed into puncta (Figure 1D). Interestingly, vimentin colocalised strongly with microtubules[35,36], and also reorganised into a dense network surrounding the nucleus following paclitaxel treatment (Figure 1E).

To visualise the rearranged cytoskeleton at high resolution and investigate how it interacts with the nucleus, we used electron cryo-tomography (cryo-ET). Cells were first thinned by cryo-focused ion beam (cryo-FIB) milling before tilt-series acquisition on the resulting lamellae. In the reconstructed tomograms, paclitaxel-treated cells frequently contained large, dense bundles of parallel microtubules and vimentin filaments which were absent from control cells (Supplementary Figure 1). These bundles could be observed to closely associate with the nuclear envelope (Figure 1F and G; Supplementary Figure 1).

Overall, these data indicate large-scale reorganisation of the cytoskeleton in the perinuclear region that could lead to changes in nuclear-cytoskeletal coupling following paclitaxel treatment.

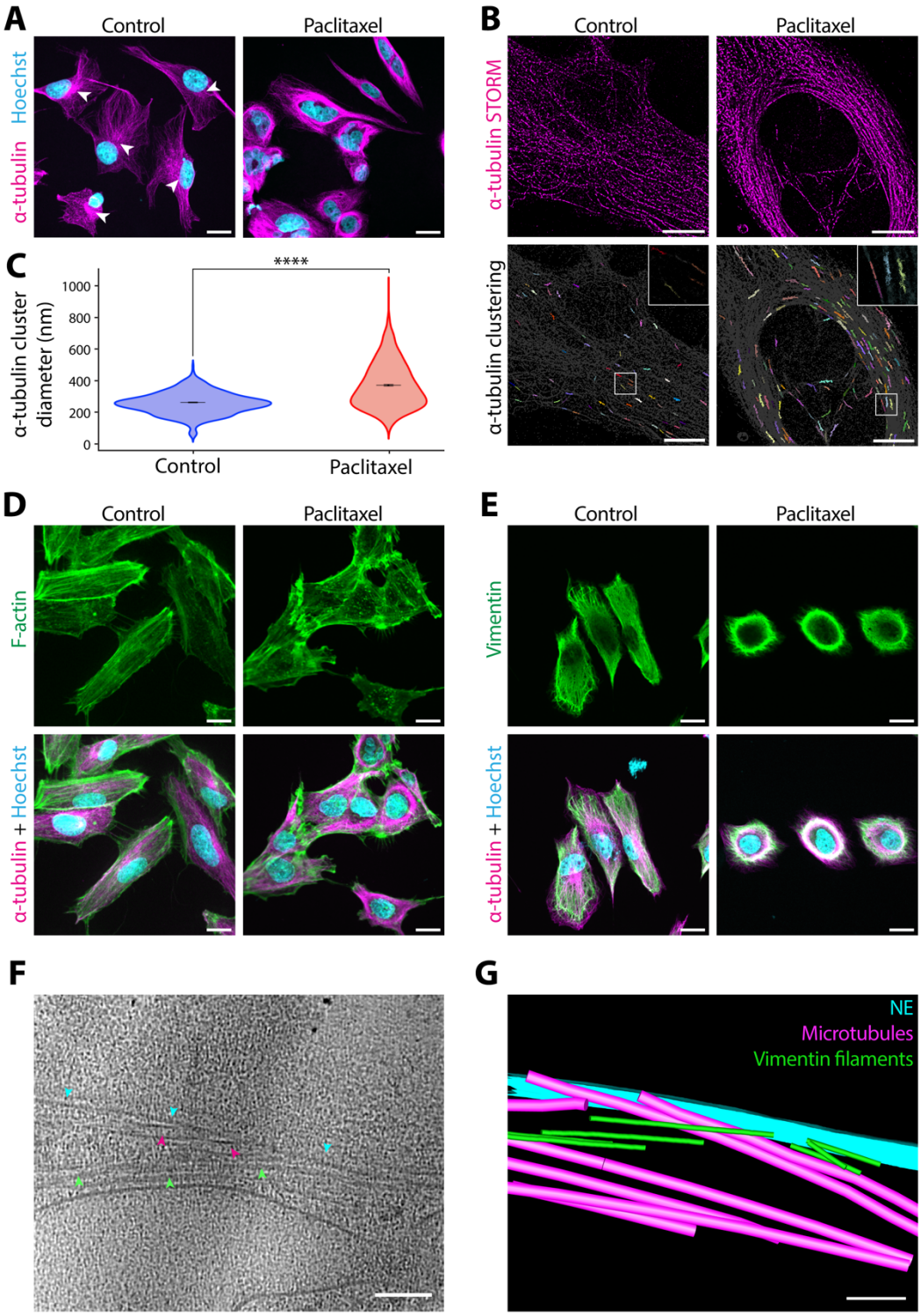

Figure 1 - Paclitaxel-induced cytoskeletal reorganisation around the nucleus in interphase. (A) Confocal micrographs of cells fixed after 16 h incubation in control media or 5 nM paclitaxel. DNA was stained using Hoechst (cyan), and microtubules using α-tubulin immunofluorescence (magenta). MTOCs are marked with arrowheads.

Scale bars = 20 µm. **(B)** STORM imaging of α-tubulin immunofluorescence in cells fixed after 16 h incubation in control media or 5 nM paclitaxel. Lower panels show α-tubulin clusters generated with HDBSCAN analysis. Scale bars = 10 µm. **(C)** Violin plot comparing the diameter of α-tubulin clusters from (B) between control cells (blue) and paclitaxel-treated cells (red). Mean ± the standard error of the mean (SEM): Control = 260 ± 3.03 nm, n = 20 cells; Paclitaxel = 369 ± 5.67, n = 20 cells. Statistical analysis: t-test, P = 3.39 x 10^{-16} (****). **(D-E)** Confocal micrographs of control and paclitaxel-treated cells stained for DNA using Hoechst (cyan), microtubules using α-tubulin immunofluorescence (magenta), and either **(D)** F-actin using Alexa488-phalloidin (green), or **(E)** vimentin using immunofluorescence (green). Scale bars = 20 µm. **(F)** 2D slice of a reconstructed tomogram of the NE region in a paclitaxel-treated cell. Bundled vimentin filaments (green arrowheads) and microtubules (magenta arrowheads) are seen closely apposed to the NE (cyan arrowheads). Scale bar = 100 nm. **(G)** Segmentation of the NE (cyan), microtubules (magenta), and vimentin filaments (green) from the tomogram in (F). Scale bar = 100 nm.

Paclitaxel-induced nuclear deformation is dependent on Lamin A/C expression levels

LINC complexes connect the cytoskeleton to the NE and underlying lamina[19]. We hypothesised that the observed cytoskeletal reorganisation would affect this mechanical coupling and force distribution to the nucleus, resulting in nuclear deformation. To test this, high content live cell imaging was performed over 48 h in the presence of 0, 1, 5, or 10 nM paclitaxel to measure nuclear solidity of nuclei in wild-type fibroblasts (Figure 2A; Supplementary Figure 2). Nuclear solidity provided a measure of nuclear deformation[37] (Supplementary Figure 3) on a scale of 0 (most deformed) to 1 (least deformed), with Hoechst used as a nuclear marker. As expected, nuclei had high nuclear solidity in the absence of paclitaxel (Figure 2A), indicating that they were not majorly deformed. In contrast, nuclear deformation increased over time in the presence of paclitaxel, and this was concentration dependent (Figure 2A; Supplementary Figure 2).

Since A-type lamins are major determinants of nuclear rigidity and the ability of the nucleus to withstand mechanical forces[38], we next tested how Lamin A/C expression levels affect paclitaxel-induced nuclear deformation. Nuclear solidity was compared between wild-type cells, cells transiently overexpressing GFP-Lamin A/C, and cells with Lamin A/C depleted using siRNA (Figure 2B and C; Supplementary Figure 4). In the absence of paclitaxel, nuclear solidity remained high across all three Lamin A/C expression levels. However, in the presence of paclitaxel, nuclear deformation was significantly greater in Lamin A/C depleted cells and significantly reduced when Lamin A/C was overexpressed (Figure 2C). Overall, this indicates that paclitaxel-induced nuclear deformation depends on Lamin A/C expression levels.

In addition to misshapen nuclei, cells containing multiple smaller nuclei, termed multimicronuclei, were observed following paclitaxel treatment (Figure 2D). Live cell imaging showed that in every instance they arose immediately following cell division, but we never observed this during interphase (Figure 2E). Importantly, quantifying the proportion of cells undergoing mitosis following 30 h incubation in 5 nM paclitaxel using immunofluorescence analysis showed that the proportion of mitotic cells in paclitaxel was 6.9 ± 0.4%, only slightly higher than that in control conditions (4.4 ± 0.6%) (Supplementary Figure 5A). Therefore, paclitaxel did not induce sustained mitotic arrest, indicating instead that cells were able to exit mitosis in the presence of clinically relevant concentrations of paclitaxel. Exit from mitosis in which the mitotic spindle is disrupted by paclitaxel likely results in chromosome mis-segregation, forming multimicronuclei following NE reformation. Consistent with this, immunofluorescence microscopy analysis of mitotic cells in paclitaxel revealed they contain disorganised mitotic spindles that were frequently multipolar, in contrast to bipolar spindles in untreated cells (Supplementary Figure 5B). The appearance of multimicronuclei in

ovarian cancer cells was previously observed to depend on decreased Lamin A/C expression levels[14]. In line with this, we found that the frequency of multimicronucleated cells after 24 h in 5 nM paclitaxel was significantly lower when Lamin A/C was overexpressed and significantly higher when Lamin A/C was knocked down compared to the wild type (Supplementary Figure 5C).

To investigate whether paclitaxel induces changes to nuclear ultrastructure in addition to overall nuclear shape deformation and multimicronucleation, cryo-FIB milling with Scanning Electron Microscopy (cryo-FIB/SEM) volume imaging was used to visualise the NE in 3D (Supplementary Figure 6). These data showed the presence of severe NE invaginations and blebs in paclitaxel-treated cells (Supplementary Figure 6). Furthermore, the separation of the inner and outer nuclear membranes (INM and ONM, respectively) also appeared to be altered (Supplementary Figure 6). In healthy cells, this distance is uniformly around 30 nm[39], but we frequently observed NE areas where the membranes appeared to have large separation or to the contrary were in very close proximity. Morphometrics analysis[40] of the NE segmented from tomograms of control and paclitaxel-treated cells was performed to quantify this (Figure 2F and G). In control cells, 67% of the NE had spacing of 20-40 nm, whereas in paclitaxel-treated cells this was decreased to 49% (Figure 2G). This was due to the significantly greater variability in the ONM-INM distance in paclitaxel-treated cells (Levene test: $P<0.0001$) because of the increased frequency of loci where the membranes were in very close proximity or highly separated, as seen in Supplementary Figure 7. Indeed, the ONM-INM distance showed a bimodal distribution in paclitaxel-treated cells, with a peak within the normal expected range at 25.5 nm and an additional peak at 10.5 nm where the two membranes were in very close proximity, in contrast to the narrow distribution around the single peak at 21.0 nm for the control (Figure 2G). Together, this indicates that perturbation to the cytoskeleton due to paclitaxel treatment results in deformation to the overall nuclear shape and to the NE, resulting in membrane invaginations and altered NE spacing.

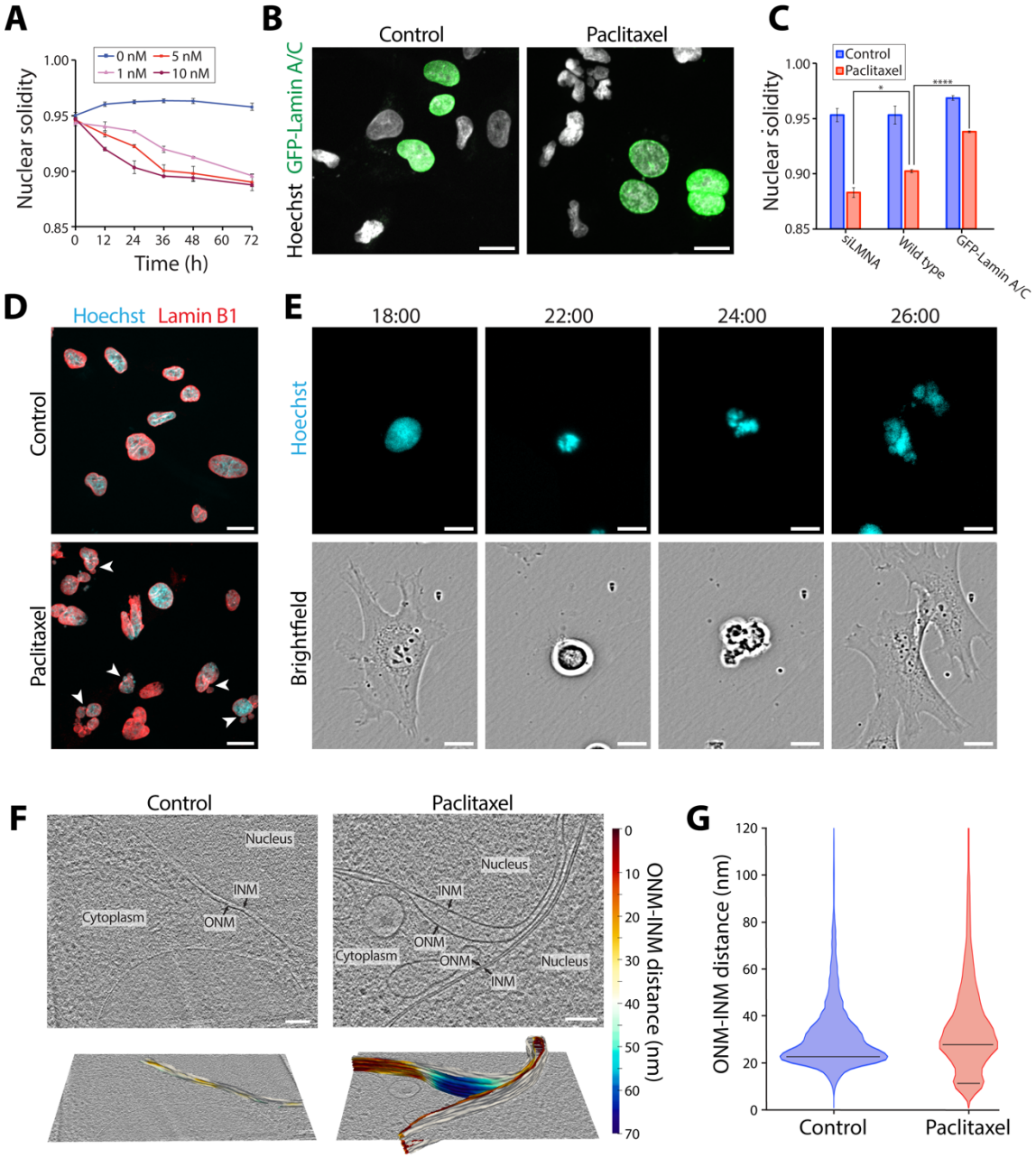

Figure 2 – Paclitaxel results in nuclear deformation. (A) Nuclear solidity of Hoechst-stained nuclei over 72 h in 0, 1, 5, or 10 nM paclitaxel. Error bars show the SEM from three biological repeats, each with more than 50 cells. **(B)** Confocal micrographs of cells transiently transfected with GFP-LMNA to overexpress GFP-Lamin A/C, fixed after 16 h incubation in control media or 5 nM paclitaxel. Cells were stained for DNA using Hoechst (white). Scale bars = 20 µm. **(C)** Nuclear solidity of Hoechst-stained nuclei from wild-type cells, cells with Lamin A/C knocked down (siLMNA), or cells with GFP-Lamin A/C overexpressed, following 16 h incubation in control media or 5 nM paclitaxel. For GFP-Lamin A/C overexpression samples, only cells expressing GFP-Lamin A/C were analysed. Error bars show SEM from three biological repeats, each with at least 30 cells. Statistical analysis: t-test; wild type paclitaxel versus siLMNA paclitaxel, P=0.0146 (*); wild type paclitaxel versus GFP-Lamin A/C paclitaxel, P=1.74 x 10^{-5} (****). **(D)** Confocal micrographs of cells fixed after 24 h incubation in control media or 5 nM paclitaxel, with the nucleus stained using Hoechst (cyan) and Lamin B1 immunofluorescence (red). Multimicronucleated cells are marked with arrowheads. Scale bars = 20 µm. **(E)** Live cell imaging showing a Hoechst-stained cell undergoing mitosis in the presence of 5 nM paclitaxel, 18-26 h after paclitaxel addition. Scale bars = 20 µm. **(F)** 2D slices of reconstructed tomograms of the NE in control and paclitaxel-treated cells. Segmentations of the ONM and INM for morphometrics analysis are shown in the lower panels, with the ONM coloured using a heatmap of the ONM-INM distance. **(G)** Violin plot comparing the ONM-INM distance between control and paclitaxel-treated cells. A total NE area of 1.64 μm^2 over 23 tomograms was analysed for the control, and 3.97 μm^2 over 41 tomograms was analysed for paclitaxel-treated cells. The black lines represent the modal values (21.0 nm for control; 10.5 nm and 25.5 nm for paclitaxel).

Paclitaxel treatment disrupts the nuclear lamina via the LINC complex protein SUN2

Next, we investigated whether the nuclear lamina is also impacted by paclitaxel treatment (Figure 3A-C; Supplementary Figure 8). As expected, immunofluorescence analysis of Lamin A/C and Lamin B1 showed both proteins were uniformly distributed around the nucleus in control cells (Figure 3A; Supplementary Figure 8). However, they were absent from certain areas of the NE following paclitaxel treatment, resulting in a patchy appearance of the nuclear lamina (Figure 3A; Supplementary Figure 8). Importantly, Western blotting revealed that total cellular levels of Lamin A/C were decreased by paclitaxel in a concentration-dependent manner (Figure 3B and C). In contrast, Lamin B1 levels were nearly unaffected (Figure 3B and C).

Lamin A/C can be phosphorylated during interphase at several sites[41], which can alter its assembly into the lamina network and overall stability[42]. Additionally, paclitaxel has been reported to result in activation of MAPKs and other kinases[43,44]. To investigate Lamin A/C phosphorylation as a possible mechanism behind the observed decrease of Lamin A/C protein levels, we tested whether Lamin A/C phosphorylation was affected by paclitaxel. Immunoblotting analysis of whole-cell lysates against phospho-Ser404, a major site of Lamin A/C phosphorylation during interphase[41], showed that the phosphorylation level remained unchanged in paclitaxel (Supplementary Figure 9). This suggests an alternative mechanism for the observed reduction in Lamin A/C levels following paclitaxel treatment.

Perturbation to Lamin A/C in paclitaxel may instead occur through its direct mechanical connection to the cytoskeleton mediated via LINC complexes[19,21]. To test this, we used confocal microscopy to analyse the co-localisation of the LINC complex components SUN1 and SUN2 with Lamin A/C (Figure 3D and E; Supplementary Figure 10). Co-localisation was quantified and compared using Li's Intensity Correlation Quotient (ICQ)[45] (Figure 3E). In control cells, both SUN proteins were uniformly distributed throughout the NE and co-localised strongly with Lamin A/C (Figure 3D and E; Supplementary Figure 10). However, following paclitaxel treatment, SUN2 was unevenly distributed at the NE resulting in a patchy appearance, retaining high co-localisation with Lamin A/C (Figure D and E; Supplementary Figure). SUN1, instead, showed significant loss of co-localisation with Lamin A/C in paclitaxel (Figure D and E; Supplementary Figure 10). Immunoblotting was then used to determine whether protein levels of SUN2 or SUN1 are altered by paclitaxel (Figure 3F and G). Similar to paclitaxel's effects on Lamin A/C, SUN2 protein levels were decreased in a concentration-dependent manner (Figure 3F and G). In contrast, SUN1 showed no significant reduction in total protein levels (Figure 3F and G). These data suggest SUN2 is selectively affected by paclitaxel treatment.

To further test whether paclitaxel-induced changes to Lamin A/C protein levels occur via their direct connection to LINC complexes and therefore the cytoskeleton, we knocked down SUN2 (Figure 3H and I; Supplementary Figure 11). Lamin A/C levels remained high across all paclitaxel concentrations tested in SUN2 knockdown cells, in contrast to the decrease of Lamin A/C levels in paclitaxel-treated wild-type cells (Figure 3H and I). This suggests that in the absence of SUN2, altered cytoskeletal forces in paclitaxel are unable to be transmitted to the nuclear lamina to perturb Lamin A/C protein levels. In contrast, when Lamin A/C is knocked down, a concentration-dependent decrease in SUN2 protein levels is still observed upon paclitaxel treatment

(Supplementary Figure 12). Altogether, these results indicate that altered cytoskeletal forces in paclitaxel are transmitted via SUN2-containing LINC complexes to the nuclear lamina, resulting in an aberrant NE.

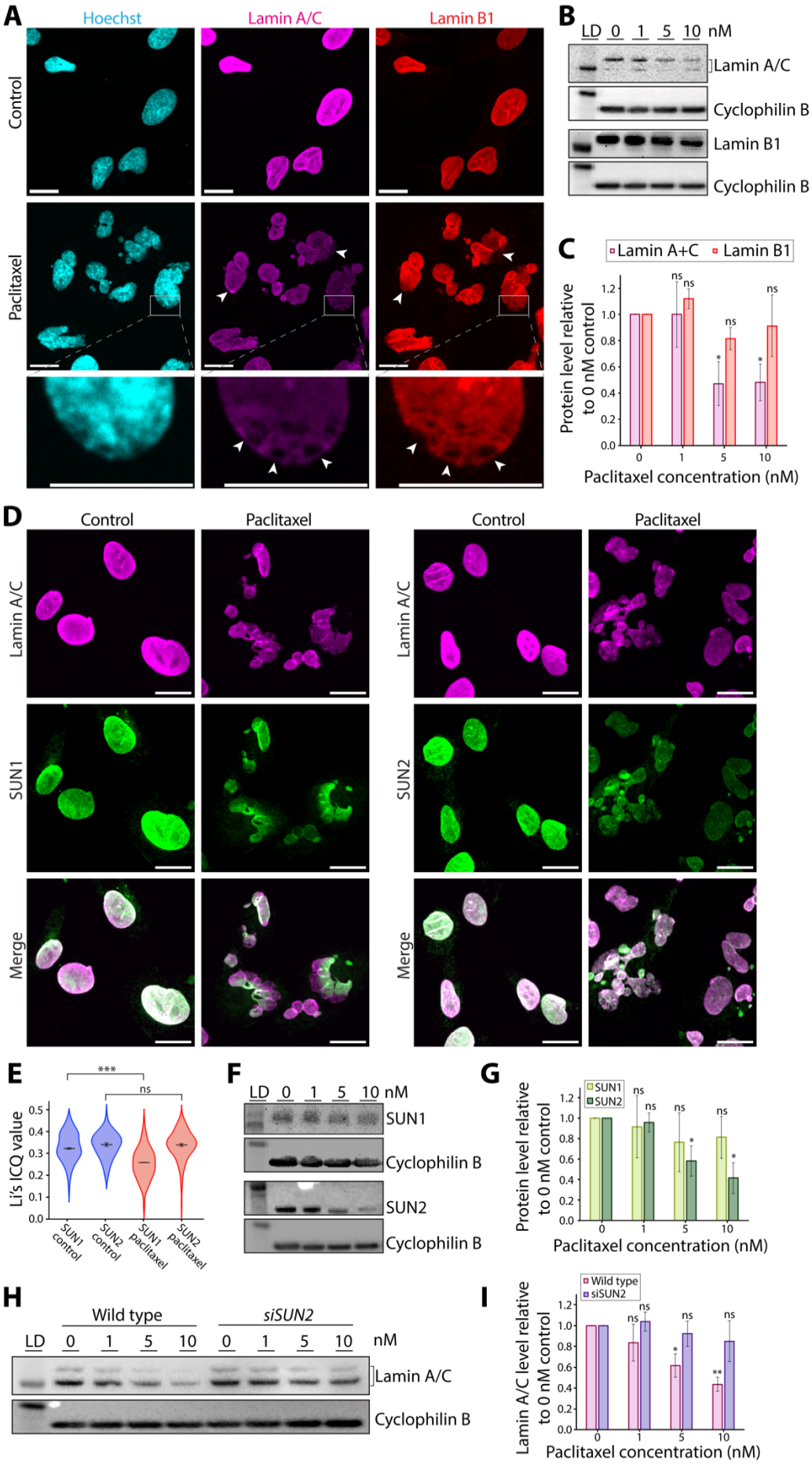
A
Hoechst
Lamin A/C
Lamin B1
Control
Paclitaxel
B
LD 0 1 5 10 nM
Lamin A/C
Cyclophilin B
Lamin B1
Cyclophilin B
C
Lamin A+C
Lamin B1
Protein level relative to 0 nM control
Paclitaxel concentration (nM)
D
Control
Paclitaxel
Lamin A/C
SUN1
SUN2
Merge
E
Li's ICQ value
SUN1 control
SUN2 control
SUN1 paclitaxel
SUN2 paclitaxel
F
LD 0 1 5 10 nM
SUN1
Cyclophilin B
SUN2
Cyclophilin B
G
SUN1
SUN2
Protein level relative to 0 nM control
Paclitaxel concentration (nM)
H
Wild type
siSUN2
LD 0 1 5 10 0 1 5 10 nM
Lamin A/C
Cyclophilin B
I
Wild type
siSUN2
Lamin A/C level relative to 0 nM control
Paclitaxel concentration (nM)

Figure 3 - Paclitaxel results in aberrations to the nuclear lamina. (A) Confocal micrographs of cells fixed after 16 h incubation in control media or 5 nM paclitaxel. DNA was stained using Hoechst (cyan), and Lamin A/C (magenta) and Lamin B1 (red) were stained using immunofluorescence. Areas of the lamina that are patchy or have Lamin A/C or B1 missing are marked with arrowheads. Lower panels show magnified views of a patchy area of the lamina, marked with a dotted rectangle. Scale bars = 20 µm. **(B)** Western blots for Lamin A/C and Lamin B1 of whole cell lysates following 16 h incubation in media containing 0, 1, 5, or 10 nM paclitaxel. Cyclophilin B was used as a loading control. Lane 1 shows protein ladder (LD; 62 kDa for Lamin A/C and Lamin B1 panels, and 28 kDa for Cyclophilin B panels). **(C)** Quantification of Lamin A/C and Lamin B1 protein levels from (B). Each band was normalised to the corresponding Cyclophilin B loading control. Error bars represent the standard deviation from three biological repeats. Statistical analysis: one sample t-test with null hypothesis mean = 1. Lamin A/C: 1 nM P=0.9971; 5 nM P=0.0314; 10 nM P=0.0232. Lamin B1: 1 nM P=0.0762; 5 nM P=0.0854; 10 nM P=0.2345. **(D)** Confocal micrographs of cells fixed after 16 h incubation in control media or 5 nM paclitaxel. Cells were stained for Lamin A/C (magenta) and either SUN1 or SUN2 (green) using immunofluorescence. Scale bars = 20 µm. **(E)** Analysis of the co-localisation between Lamin A/C and SUN1 or SUN2 from (D). Fluorescence colocalization was quantified using Li's ICQ value[45], where more positive values represent better positive colocalization. Error bars represent the SEM from 3 biological repeats, each with more than 30 cells. Statistical analysis: t-test control versus paclitaxel. SUN1: P=0.0002. SUN2: P=0.8788. **(F)** Western blots for SUN1 and SUN2 of whole cell lysates following 16 h incubation in media containing 0, 1, 5, or 10 nM paclitaxel. Cyclophilin B was used as a loading control. Lane 1 shows protein ladder (LD; 98 kDa for SUN1 and SUN2 panels, and 28 kDa for Cyclophilin B panels). **(G)** Quantification of SUN1 and SUN2 protein levels from (F). Each band was normalised to the corresponding Cyclophilin B loading control. Error bars represent the standard deviation from three biological repeats. Statistical analysis: one sample t-test with null hypothesis mean = 1. SUN1: 1 nM P=0.6816; 5 nM P=0.2948; 10 nM P= 0.2548. SUN2: 1 nM P=0.5320; 5 nM P=0.0395; 10 nM P= 0.0214. **(H)** Western blots for Lamin A/C of whole cell lysates from wild-type or SUN2-knockdown (siSUN2) cells following 16 h incubation in 0, 1, 5, or 10 nM paclitaxel. Cyclophilin B was used as a loading control. Lane 1 shows protein ladder (LD; 62 kDa for Lamin A/C panel, and 28 kDa for Cyclophilin B panel). **(I)** Quantification of Lamin A/C protein levels from (H). Each band was normalised to the corresponding Cyclophilin B loading control. Error bars represent the standard deviation from three biological repeats. Statistical analysis: one sample t-test with null hypothesis mean = 1. Wild type: 1 nM P=0.2455; 5 nM P=0.0271; 10 nM P=0.0046. siSUN2: 1 nM P=0.5481; 5 nM P=0.3769; 10 nM P=0.3137. Ns = non-significant = P>0.05; * P<0.05; ** P<0.01; *** P<0.001; **** P<0.0001.

Lamin A/C expression levels determine sensitivity to paclitaxel treatment

As Lamin A/C expression levels determine nuclear deformation in paclitaxel, we then tested how this relates to overall sensitivity to paclitaxel. High-content screening was used to quantify cell confluency of the wild type, Lamin A/C knockdown, and GFP-Lamin A/C overexpression over 48 h in 0, 1, 5, or 10 nM paclitaxel (Figure 4A). Without paclitaxel, cell growth was similar across all three Lamin A/C expression levels tested. In 1 and 5 nM paclitaxel, cell growth was reduced, but to a lesser extent when Lamin A/C was overexpressed compared to the wild type and Lamin A/C knockdown (Figure 4A). In 10 nM paclitaxel, cell confluency remained low across all three Lamin A/C expression levels (Figure 4A) as the high concentration prevented almost any cell growth.

Next, the effects of Lamin A/C expression levels on cell viability in paclitaxel were tested (Figure 4B). Cell viability was determined by calculating the proportion of the total number of cells that were dead or apoptotic, with these cells identified using the caspase 3 and 7 dye FLICA (Supplementary Figure 13). Increasing concentrations of paclitaxel resulted in lower cell viability, and this was more pronounced in Lamin A/C depleted cells (Figure 4B). However, at high concentrations of paclitaxel (10 nM), Lamin A/C knockdown no longer had an observable impact on cell viability. Conversely, cells overexpressing Lamin A/C displayed higher cell viability in paclitaxel, even at high concentrations (Figure 4B). Overall, these data indicate that Lamin A/C expression levels affect sensitivity to paclitaxel in terms of both cell growth and cell death.

Finally, we tested whether cells recover from paclitaxel treatment. Immunofluorescence confocal microscopy showed that microtubule organisation

returned to normal following paclitaxel removal, and so did the localisation of Lamin B1 and Lamin A/C (Supplementary Figure 14). Lamin A/C and SUN2 protein levels also recovered, as determined by Western blotting (Supplementary Figure 15).

However, since Lamin A/C expression levels affect cell sensitivity to paclitaxel (Figure 4A and B), recovery from paclitaxel may also depend on Lamin A/C expression levels. To test this, cell confluency of wild-type and Lamin A/C knockdown cells was quantified following removal of 5 nM paclitaxel (Figure 4C). Whereas wild-type cells expanded in cell number following paclitaxel removal, Lamin A/C knockdown cells showed little cell growth (Figure 4C). Altogether, this shows that Lamin A/C expression levels also affect recovery from paclitaxel, in addition to cell death and inhibition of cell growth.

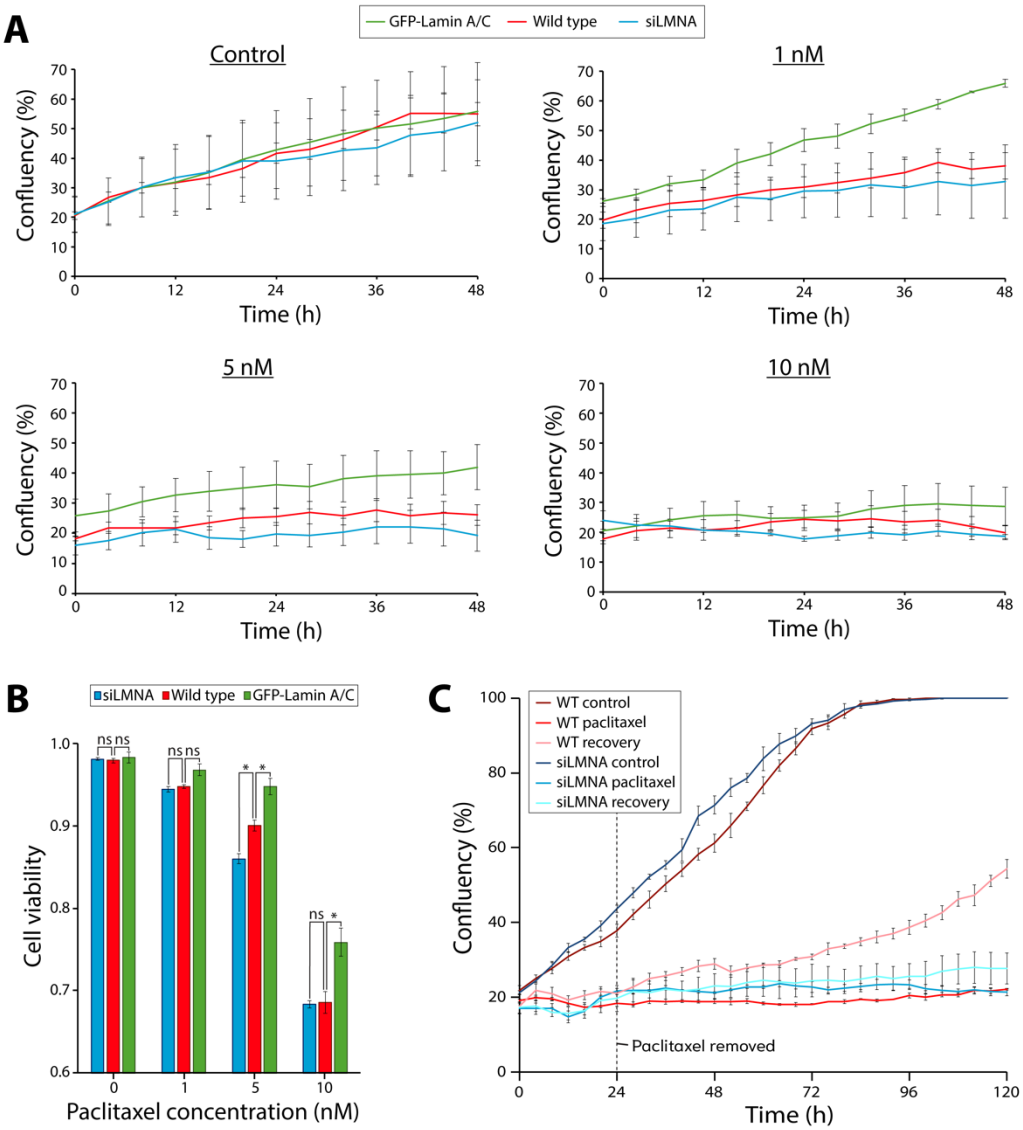

Figure 4 – Lamin A/C expression level affects cell sensitivity to and recovery from paclitaxel. (A) Cell confluency of wild-type (red), GFP-Lamin A/C overexpression (green), and Lamin A/C knockdown (blue) cells over 48 h in 0, 1, 5, or 10 nM paclitaxel. Confluency was calculated from brightfield high-content live cell images. Error bars represent the SEM from three biological repeats. **(B)** Bar graph comparing cell viability between wild-type (red), GFP-Lamin A/C overexpression (green), and Lamin A/C knockdown (blue) cells following 20 h incubation in 0, 1, 5, or 10 nM paclitaxel. Cell viability was calculated by subtracting the proportion of the total number of cells that were dead/apoptotic (identified by FLICA staining) from 1. Error bars represent SEM from three biological repeats, each with more than 150 cells. Statistical analysis: t-test versus wild type. 0 nM: siLMNA P= 0.5450; GFP-Lamin A/C P= 0.5809. 1 nM: siLMNA P= 0.4454; GFP-Lamin A/C P= 0.0597. 5 nM: siLMNA P= 0.0110; GFP-Lamin

A/C P= 0.0169. 10 nM: siLMNA P= 0.8643; GFP-Lamin A/C P= 0.0290. Ns (non-significant) = P>0.05; * = P<0.05. **(C)** Cell confluency of wild-type and Lamin A/C knockdown cells in control media (control), media with the sustained presence of 5 nM paclitaxel (paclitaxel), or media from which paclitaxel was removed after 24 h (recovery).

Discussion

Despite its widespread use, the mechanism by which paclitaxel selectively kills cancer cells is not yet fully understood. A better understanding of paclitaxel's effects is therefore important for improving treatment and reducing drug resistance and toxicity. In this study, we investigated how paclitaxel disrupts nuclear-cytoskeletal coupling during interphase. We show that paclitaxel treatment results in nuclear aberrations, including NE deformation, multimicronucleation, and disruption to the nuclear lamina via SUN2-containing LINC complexes. Cells with lower Lamin A/C expression levels, typical of many different cancer cells[27–31], showed increased sensitivity to paclitaxel in terms of cell growth, death, and recovery, indicating how disrupted nuclear-cytoskeletal coupling can lead to a selective targeting of cancer cells, even in slowly proliferating tumours.

Previously, the anti-cancer activity of paclitaxel was thought to rely mostly on the activation of the mitotic checkpoint through disruption of microtubule dynamics, ultimately resulting in apoptosis. Evidence for this came from *in vitro* cell culture and xenograft models which rely on cells with extensive replicative capacity and short doubling times[7,46–48]. However, these cells may be more vulnerable to disruption of mitosis than tumour cells in patients, which can have longer doubling times[11,49]. For its activity against these cancers, paclitaxel must therefore have anti-cancer effects outside of mitosis. In support of this, drugs that specifically block mitosis have not been successful in the clinic[11], indicating that the efficacy of microtubule-targeting drugs like paclitaxel comes from effects in interphase in addition to mitosis. Furthermore, tumour biopsies from breast cancer patients treated with microtubule stabilising drugs show that mitotic cells are rare, despite patient response to therapy[11,50]. One alternative hypothesis to explain this lack of mitotic cells in paclitaxel-treated tumour samples is that at intratumoral concentrations, cells undergoing mitosis can escape the mitotic checkpoint, and this mitotic slippage results in multimicronucleation and subsequently apoptosis[7]. Multimicronucleation has been observed previously in ovarian cancer cells following paclitaxel treatment and this was proposed to occur during interphase as a consequence of aberrant cytoskeletal forces[14]. In contrast with this, we show that paclitaxel also induces multimicronucleation in healthy human fibroblasts and that it always occurs during exit from mitosis (Figure 2E). Interestingly, we observed that the mitotic index of human fibroblasts remains low in paclitaxel (Supplementary Figure 5A), indicating that cells can exit from mitosis at clinically-relevant concentrations of paclitaxel. However, the frequency of multimicronucleation depended on Lamin A/C expression levels (Supplementary Figure 5C), as observed previously[14]. This is likely explained by the important role the nuclear lamina plays in the fragmentation and reassembly of nuclear membranes during mitosis[51,52]. NE reformation around aberrantly segregated chromosomes could therefore be affected by Lamin A/C expression levels, explaining the differences in multimicronucleation frequency.

However, multimicronucleation alone cannot account for paclitaxel's activity against tumours with slow duplication rates[8–10], as it is unlikely that enough cells undergo mitosis in paclitaxel for this mechanism to be sufficient. This is supported by intravital imaging of tumours in mice treated with docetaxel, another taxane similar to paclitaxel,

which demonstrated that apoptosis is induced in most tumour cells independently of mitotic defects, including both mitotic arrest and multimicronucleation[9].

Previously, paclitaxel was shown to affect microtubule organisation in interphase cells in a cell-type specific manner, with some cells containing microtubule rings around the nucleus while others contain multiple microtubule asters[13]. Here, we show that paclitaxel promotes the formation of dense bundles of microtubules and vimentin filaments surrounding the interphase nucleus in human fibroblasts (Figure 1 and Supplementary Figure 1) , which coincide with nuclear deformation and NE invaginations (Figure 2A and F; Supplementary Figure 6). Because vimentin becomes upregulated during the epithelial-to-mesenchymal transition[53] and so it is commonly overexpressed in cancer cells[54], these cytoskeletal rearrangements in fibroblasts likely mirror those in cancer cells. Since paclitaxel-treated cells lack prominent actin stress fibres adjacent to the nucleus[12] (Figure 1D), nuclear deformation likely occurs via the microtubule and vimentin cytoskeletons. Indeed, microtubules connect to LINC complexes in the NE via interactions between the microtubule motors kinesin and dynein and the N-terminus of KASH proteins[55,56], while vimentin filaments connect to KASH proteins via plectin[57]. Furthermore, perinuclear assemblies of both microtubules and vimentin filaments have been previously observed to induce nuclear deformation in interphase[58,59]. The large, dense filament bundles in paclitaxel-treated cells may exert force on the nucleus either directly via steric effects or via their mechanical connection to LINC complexes[55–57].

LINC complexes in turn connect to the nuclear lamina in the nucleoplasm[21,60]. Here, we show that paclitaxel treatment decreases Lamin A/C expression levels (Figure 3B and C). In other systems, Lamin A/C levels respond to mechanical cues[61], and this mechanosensing is thought to be achieved through post-translational modifications of Lamin A/C, including phosphorylation, acetylation, and ubiquitylation[62–64]. In particular, Lamin A/C phosphorylation regulates its assembly and stability in the nuclear lamina and its subsequent degradation[41,42]. Phosphorylation is not the mechanism through which Lamin A/C levels are decreased in paclitaxel (Supplementary Figure 9). Instead, we postulate a different mechanism involving the direct connection of Lamin A/C to SUN2-containing LINC complexes. The role of LINC complexes in paclitaxel-induced nuclear lamina perturbations is further supported by the fact that Lamin A/C but not Lamin B1 levels are decreased (Figure 3B and C). This is because, in contrast to robustly expressed Lamin B1 which is not mechanically linked to the cytoskeleton directly via LINC complexes[21,65], Lamin A/C is directly connected to LINC complexes[21,60], and its expression and turnover are known to be controlled by tissue stiffness and mechanical stress[61,65].

A role for LINC complexes in paclitaxel-induced nuclear deformation is further supported by the uneven localisation and decreased protein levels of SUN2 (Figure 3D, F and G). This aberrant SUN2 localisation in the NE likely also accounts for the altered nuclear membrane spacing in paclitaxel (Figure 2F and G; Supplementary Figure 7). Since SUN proteins in LINC complexes contain perinuclear coiled-coil domains of a set length (~45 nm for SUN2-containing LINC complexes)[66], their presence in the NE controls the inter-membrane distance within narrow limits[60,66]. This control is lost when SUN proteins are absent[60], enabling the two membranes to be more easily forced together or separated under cytoskeletal forces, as observed here (Figure 2F and G). SUN1 is still present in paclitaxel-treated cells, and this likely

explains why a large proportion of the NE has spacing within the expected range of 20-40 nm (Figure 2G). However, its expression levels remain the same and therefore SUN1 is unlikely to be able to completely compensate for the absence of SUN2, explaining the increased variability in NE spacing in paclitaxel-treated cells (Figure 2G).

It is still unclear why SUN2 and not SUN1 is specifically disrupted by mechanical perturbation[67] and paclitaxel treatment (Figure 3F and G). However, mechanical perturbations in the form of cyclic tensile strain have previously been shown to decrease levels of SUN2, but not SUN1, in human mesenchymal stem cells[67]. We show that this decrease in SUN2 levels occurs independently of Lamin A/C (Supplementary Figure 12). Instead, one possibility is that SUN2 is more readily turned over by proteasomal degradation following disruption to the NE. It has been shown previously that the turnover of SUN2 but not SUN1 is important in the control of nuclear mechanics, in particular nuclear shape[68]. This occurs via ubiquitination by the E3 ubiquitin ligase $SCF^{\beta TrCP}$, which recognises a $SCF^{\beta TrCP}$ recognition site in SUN2 that is absent from SUN1[68]. This selective degradation may explain why protein levels of SUN2 but not SUN1 are decreased by paclitaxel treatment (Figure 3F and G).

Although both SUN1 and SUN2 have been shown to interact directly with Lamin A/C[60], upon paclitaxel treatment, SUN2 and Lamin A/C co-localised well whereas SUN1 did not (Figure 3D and E). This specific co-localisation indicates that SUN2 might be the main mediator of mechanical connections between Lamin A/C and microtubules and/or vimentin filaments in human fibroblasts. We propose that these mechanical connections are what drive perturbations to Lamin A/C in paclitaxel (Figure 3A-C; Supplementary Figure 8). Supporting this, the paclitaxel-induced decrease of Lamin A/C protein levels was no longer observed when SUN2 was knocked down (Figure 3H and I). This suggests that in the absence of SUN2-containing LINC complexes, aberrant cytoskeletal forces are no longer effectively transmitted to Lamin A/C to perturb its protein levels and localisation at the nuclear lamina.

Disruption to the nuclear lamina and NE observed in paclitaxel likely compromises the ability of the nucleus to buffer cytoskeletal forces, resulting in loss of nuclear integrity, widespread DNA damage, and, if severe enough, cell death[17,69–71]. Consequently, cells already containing a defective nuclear lamina or NE may be more susceptible to these effects. Indeed, we showed that Lamin A/C knockdown increases the severity of nuclear deformation in paclitaxel (Figure 2B and C) as well as the frequency of multimicronucleation (Supplementary Figure 5C), and results in increased cell death, decreased cell growth, and decreased recovery from paclitaxel (Figure 4). Since nuclear abnormalities are common across most cancer types[26,31], particularly alterations to the nuclear lamina and decreased Lamin A/C levels[27–31], this study provides an explanation for the selective targeting of cancer cells by paclitaxel during interphase.

Overall, our study presents a novel mechanism for the anti-cancer activity of paclitaxel in interphase, whereby cancer cells show increased sensitivity to nuclear deformation induced by aberrant nuclear-cytoskeletal coupling. Therefore, we conclude that paclitaxel functions in interphase as well as mitosis, elucidating how slowly growing tumours are targeted[8–10]. Since better understanding the mechanisms of paclitaxel and its effects on nuclear architecture is important for its safe and efficacious use as

an anti-cancer drug, our study might inform patient stratification, and the development of safer drug formulations. Similarly, our findings may be relevant for the search and/or design of other drugs that affect nuclear-cytoskeletal coupling.

Materials and methods

Cell culture and paclitaxel treatment

Human telomerase reverse transcriptase (hTERT) immortalised human fibroblasts were cultured at 37°C and 5% CO_2 in complete medium consisting of Dulbecco's modified Eagle's medium (DMEM) with GlutaMAX (Gibco), supplemented with 10% fetal bovine serum (Gibco) and 1% penicillin/streptomycin (Gibco).

For paclitaxel treatment, paclitaxel (Merck PHL89806) resuspended in dimethyl sulfoxide to 10 mM was diluted in complete DMEM to final concentrations of 1, 5, or 10 nM as indicated. Controls consisted of untreated cells.

Transfections, and RNA interference

To overexpress Lamin A/C, cells were transfected for 5 h using Lipofectamine 3000 (Invitrogen) with 0.5 µg pBABE plasmid expressing GFP-LMNA. Overexpression was confirmed by fluorescence microscopy (Figure 2B). For knockdowns, cells were transfected with the indicated small interfering RNA (siRNA) at a final concentration of 100 nM using lipofectamine 3000 (Supplementary Table 1). Knockdown was confirmed using Western blot analysis (Supplementary Figure 4 and 11). Drug treatments were started 2 days after transfection.

High-content live cell imaging

Cells adhered to 24-well plates (Corning) were stained for 10 min with Hoechst 33342 (ThermoFisher) diluted by 1:10,000 in complete medium. The indicated concentration of paclitaxel was then added, and 24-well plates were transferred to CELLCYTE X Live Cell Imager (Cytena) fitted with a 10X objective lens (air, NA 0.3) held at 37°C and 5% CO_2 and imaged every 2 h. For paclitaxel recovery, wells were washed and the media replaced with complete medium after 24 h.

To quantify nuclear shape deformation, images were transferred to ImageJ for analysis and Hoechst-stained nuclei were selected by threshold and the 'analyse particles' function used to calculate nuclear solidity. Nuclei that were overlapping with those from adjacent cells or that were within dead cells, identified by their distinctive cell shape, were excluded from the analysis.

Cell growth was quantified by measuring confluency from brightfield images using the automated image analysis tool in CELLCYTE X (Cytena).

Cell staining and immunofluorescence

Following transfection and/or paclitaxel treatment, cells adhered on #1.5 glass coverslips were stained with Hoechst 33342 at 1:10,000 in complete medium for 10 min at 37°C. Cells were then washed with PBS, fixed with 4% paraformaldehyde for 15 min at room temperature, then washed with PBS before autofluorescence was quenched using 50 mM ammonium chloride. Cells were then permeabilised and blocked in permeabilization buffer (0.1% Triton X-100 and 2% bovine serum albumin in PBS) for 30 min then washed in PBS. Cells were then incubated at room

temperature for 1 h in permeabilization buffer with the indicated primary antibodies (Supplementary Table 2) or Alexa488 phalloidin (1:400; Invitrogen). After washing with PBS, cells were incubated at room temperature for 1 h in secondary antibodies in permeabilization buffer (Supplementary Table 2) then washed with PBS. For STORM samples, cells were then incubated with 4% paraformaldehyde for 10 min then washed and stored in PBS. Otherwise, cells were mounted using Prolong Gold (ThermoFisher).

For quantification of cell viability, cells adhered on #1.5 glass coverslips were stained with Hoechst 33342 at 1:10,000 in complete medium for 10 min at 37ºC after the indicated paclitaxel treatment. Cells were then washed with complete medium twice, then stained for active caspases 3 and 7 using FLICA reagent from Image-iT LIVE Red Caspase Detection Kit (Invitrogen). Cells were then washed twice, fixed with 4% paraformaldehyde for 15 min at room temperature, washed with PBS, then mounted. Following confocal microscopy, the proportion of dead or apoptotic cells was calculated by measuring the proportion of cells that were stained using FLICA.

Light microscopy

Immunofluorescence imaging was performed using NIS-Elements software and a Nikon X1 Spinning Disk inverted microscope equipped with a 40X objective lens (oil immersion, numerical aperture [NA] 1.3) and sCMOS camera.

For Stochastic Optical Reconstruction Microscopy (STORM), immunofluorescence samples were immersed in STORM buffer (10% glucose, 10 mM sodium chloride, 50 mM Tris-HCl pH 8.0, 5.6 % glucose oxidase, 3.4 mg/ml catalase, 0.1% 2-mercaptoethanol) and imaged using a Nanoimager system (ONI) equipped with a 100X TIRF objective lens (oil immersion, NA 1.49). For imaging, Highly Inclined and Laminated Optical Sheet (HILO) illumination was used with laser power 60-150 mW, and 15,000 frames were acquired. CODI software (ONI) was used for image processing, including drift correction and HDBSCAN clustering. For α-tubulin cluster analysis, HDBSCAN clusters were constrained to have a minimum number of 15 localisations, maximum circularity of 0.5, and minimum length of 1000 nm so that the clusters mapped to individual filament bundles.

Western blotting

Cells were collected by treatment with 0.25% trypsin-EDTA for 3 min then dilution in PBS followed by centrifugation at 400 x g for 10 min. Cells were lysed with 1X NUPAGE LDS sample buffer (Invitrogen) supplemented with 50 mM dithiothreitol. After boiling at 95ºC for 10 min, proteins were separated using NUPAGE 4-12% Bis-Tris gels (ThermoFisher) in MES SDS buffer alongside a protein ladder (Invitrogen SeeBlue Plus2). Proteins were transferred to PVDF membranes (BioRad) which were then incubated in blocking buffer (5% milk power and 0.1% Tween 20 in Tris-buffered saline [TBS]). The membranes were then incubated in primary antibodies in blocking buffer (Supplementary Table 2), then washed with washing buffer (1% milk and 0.1% Tween 20 in TBS), then incubated with secondary antibodies in blocking buffer (Supplementary Table 2), then washed in washing buffer again. The membranes were then activated using ECL (Cytiva) then imaged using a BioRad Chemidoc MP. Relative protein levels were quantified in ImageJ from three biological repeats, with normalisation to Cyclophilin B loading controls.

EM grid preparation
Quantifoil R 1/4 Au 200 mesh grids (Quantifoil Micro Tools GmbH) were glow discharged for 40 s at 30 mA with an Edwards S150B glow discharger then coated using 0.1 mg/ml poly-L-lysine for 30 min. Grids were then washed in PBS three times, then cells were seeded and allowed to adhere overnight, before 16 h treatment with 5 nM paclitaxel or control media. Grids were then transferred to a Leica GP2 plunger at 25°C and 95% humidity and incubated with 3.5 µl 10% glycerol as a cryo-protectant for 20 s. After 9 s blotting, grids were plunge frozen in liquid ethane.

Cryo-focussed ion beam (FIB) milling and scanning electron microscopy (SEM)
To prepare lamellae for cryo-ET acquisition, cryo-FIB milling was performed using a Scios dual beam FIB/SEM (Thermo Fisher Scientific) equipped with a PP3010T cryo stage and loading system (Quorum Technologies) according to previously published protocols[72]. Briefly, the grids were sputter-coated with an inorganic platinum layer at 10 mA for 15 s using the Quorum system sputter coater, then coated with an organometallic platinum layer (trimethyl [(1,2,3,4,5-ETA.)-1 methyl-2, 4-cyclopentadien-1-YL] platinum) using the Scios gas injection system (GIS). Milling was conducted at an angle of 10° relative to the grid in a stepwise manner with decreasing currents (0.5 nA, 0.3 nA, 0.1 nA, 30 pA), resulting in lamellae with a final width of 10-12 µm and thickness of 120-200 nm.

For volume imaging, cryo-FIB/SEM was performed using a Crossbeam 550 (Zeiss GmbH), equipped with a PP3010Z cryo stage and loading system (Quorum Technologies). Grids were sputter- and GIS-coated as above. For each cell imaged, the top of the cell was milled away using a FIB current of 3 nA until the nucleus could be observed in the SEM. The exposed surface was then milled at an angle of 7° relative to the grid with a current of 700 pA and slice thickness of 25 nm, and imaged using the SEM InLens detector at 2.3 kV, line averaging of 24, and XY pixel size of 5-6 nm/pixel.

Volume images were processed in ImageJ. First, contrast-limited adaptive histogram equalization was used to enhance contrast[73], then images in the volume stack were aligned using the SIFT algorithm[74]. Horizontal curtain stripes were then removed by horizontal stripe suppression during bandpass filtering.

Electron cryo-tomography and morphometrics analysis
Lamellae were imaged using a Titan Krios (TFS) equipped with a Gatan BioQuantum energy-filter and Gatan K3 direct electron detector. Tilt series were collected using SerialEM[75] with PACE-tomo[76] in a dose-symmetric scheme between ± 60° relative to the lamella in 3° increments. The total dose for each tilt series was ~100 e/Å^2, distributed evenly across each 12-frame tilt. The pixel size was 1.63 Å/pixel and defocus -3 to -5 µm.

For tomogram reconstruction, movies were imported into Warp[77] for gain and motion correction, tilt selection, and CTF estimation. Tomograms were then reconstructed and deconvolved following tilt series alignment using AreTomo[78].

Microtubules, vimentin filaments, and the inner and outer nuclear membranes were manually segmented in IMOD[79]. To analyse NE morphology, the NE segmentations

were then converted to 3D voxel segmentations using the 'imodmop' program within IMOD. A surface morphometrics pipeline[40] was then used to generate surface meshes of the inner and outer NEs from the 3D voxel segmentations and subsequently measure the distances between these meshes, giving the INM-ONM distance.

Acknowledgements

We thank David Barford and Barford lab members for in-depth discussions and critical feedback. We thank Delphine Larrieu for providing hTERT human skin fibroblasts. We thank Andrew Carter, Laura Machesky, and Oliver Knowles for insightful scientific discussions. We thank the cryo-EM Facility at the LMB for maintaining the electron microscopes, the Scientific Computing facility for maintaining our computer cluster and the Light Microscopy Facility for technical support with light microscopy experiments. We also acknowledge Diamond for access to the Aquilos-II of the UK national electron Bio-Imaging Centre (eBIC).

This work was supported by the Medical Research Council, as part of United Kingdom Research and Innovation (also known as UK Research and Innovation) [MC_UP_1201/30]. For the purpose of open access, the MRC Laboratory of Molecular Biology has applied a CC BY public copyright licence to any Author Accepted Manuscript version arising.

M.A. was funded by the UKRI Medical Research Council (MC_UP_1201/30), A.d.S. was funded by the Wellcome Trust Early Career Award (227622/Z/23/Z).

Author contributions

T.H., A.d.S., and M.A. conceived and designed the experiments; T.H. performed all the experiments supervised by A.d.S.; T.H. and A.d.S performed cryo-FIB milling and SEM; P.K. supported immunoblotting work and data analysis; V.L.H. supported cryo-ET work and data analysis; T.H., A.d.S., and M.A. wrote the manuscript; A.d.S. and M.A. supervised the entire study.

Declaration of interests

The authors declare no competing interests.

References

1. Ozols, R. F. *et al.* Phase III trial of carboplatin and paclitaxel compared with cisplatin and paclitaxel in patients with optimally resected stage III ovarian cancer: A Gynecologic Oncology Group study. *Journal of Clinical Oncology* **21**, 3194–3200 (2003).
2. Ranson, M. *et al. Randomized Trial of Paclitaxel Plus Supportive Care Versus Supportive Care for Patients With Advanced Non-Small-Cell Lung Cancer*. https://academic.oup.com/jnci/article/92/13/1074/2909527.

3. Bishop, J. F. *et al. Initial Paclitaxel Improves Outcome Compared With CMFP Combination Chemotherapy as Front-Line Therapy in Untreated Metastatic Breast Cancer*. *Journal of Clinical Oncology* vol. 17 (1999).
4. Xiao, H. *et al.* Insights into the mechanism of microtubule stabilization by Taxol. *Proceedings of the National Academy of Sciences* **103**, 10166–10173 (2006).
5. Schiff, P. B. & Horwitz, S. B. Taxol stabilizes microtubules in mouse fibroblast cells. *Proceedings of the National Academy of Sciences* **77**, 1561–1565 (1980).
6. Turner, P. F. & Margolis, R. L. Taxol-induced bundling of brain-derived microtubules. *J Cell Biol* **99**, 940–946 (1984).
7. Jordan, M. A., Toso, R. J., Thrower, D. & Wilson, L. Mechanism of mitotic block and inhibition of cell proliferation by taxol at low concentrations. *Proceedings of the National Academy of Sciences* **90**, 9552–9556 (1993).
8. Milross, C. G. *et al.* Relationship of Mitotic Arrest and Apoptosis to Antitumor Effect of Paclitaxel. *JNCI Journal of the National Cancer Institute* **88**, 1308–1314 (1996).
9. Janssen, A., Beerling, E., Medema, R. & van Rheenen, J. Intravital FRET Imaging of Tumor Cell Viability and Mitosis during Chemotherapy. *PLoS One* **8**, e64029 (2013).
10. Orth, J. D. *et al.* Analysis of Mitosis and Antimitotic Drug Responses in Tumors by *In Vivo* Microscopy and Single-Cell Pharmacodynamics. *Cancer Res* **71**, 4608–4616 (2011).
11. Komlodi-Pasztor, E., Sackett, D., Wilkerson, J. & Fojo, T. Mitosis is not a key target of microtubule agents in patient tumors. *Nat Rev Clin Oncol* **8**, 244–250 (2011).
12. Rosenblum, M. D. & Shivers, R. R. 'Rings' of F-actin form around the nucleus in cultured human MCF7 adenocarcinoma cells upon exposure to both taxol and taxotere. *Comp Biochem Physiol C Pharmacol Toxicol Endocrinol* **125**, 121–131 (2000).
13. Banerjee, S., Fallis, A. G. & Brown, D. L. Differential effects of taxol on two human cancer cell lines. *Oncol Res* **9**, 237–48 (1997).
14. Smith, E. R., Leal, J., Amaya, C., Li, B. & Xu, X.-X. Nuclear Lamin A/C Expression Is a Key Determinant of Paclitaxel Sensitivity. *Mol Cell Biol* **41**, (2021).
15. Theodoropoulos, P. A. *et al.* Taxol affects nuclear lamina and pore complex organization and inhibits import of karyophilic proteins into the cell nucleus. *Cancer Res* **59**, 4625–33 (1999).
16. Denais, C. M. *et al.* Nuclear envelope rupture and repair during cancer cell migration. *Science (1979)* **352**, 353–358 (2016).
17. Cho, S. *et al.* Mechanosensing by the Lamina Protects against Nuclear Rupture, DNA Damage, and Cell-Cycle Arrest. *Dev Cell* **49**, 920-935.e5 (2019).
18. Takaki, T. *et al.* Actomyosin drives cancer cell nuclear dysmorphia and threatens genome stability. *Nat Commun* **8**, 16013 (2017).
19. Starr, D. A. & Fridolfsson, H. N. Interactions Between Nuclei and the Cytoskeleton Are Mediated by SUN-KASH Nuclear-Envelope Bridges. *Annu Rev Cell Dev Biol* **26**, 421–444 (2010).
20. Mellad, J. A., Warren, D. T. & Shanahan, C. M. Nesprins LINC the nucleus and cytoskeleton. *Curr Opin Cell Biol* **23**, 47–54 (2011).

21. Haque, F. *et al.* SUN1 Interacts with Nuclear Lamin A and Cytoplasmic Nesprins To Provide a Physical Connection between the Nuclear Lamina and the Cytoskeleton. *Mol Cell Biol* **26**, 3738–3751 (2006).
22. Bouzid, T. *et al.* The LINC complex, mechanotransduction, and mesenchymal stem cell function and fate. *J Biol Eng* **13**, 68 (2019).
23. Lammerding, J. *et al.* Lamins A and C but Not Lamin B1 Regulate Nuclear Mechanics. *Journal of Biological Chemistry* **281**, 25768–25780 (2006).
24. Dahl, K. N., Kahn, S. M., Wilson, K. L. & Discher, D. E. The nuclear envelope lamina network has elasticity and a compressibility limit suggestive of a molecular shock absorber. *J Cell Sci* **117**, 4779–4786 (2004).
25. Burke, B. & Stewart, C. L. The nuclear lamins: flexibility in function. *Nat Rev Mol Cell Biol* **14**, 13–24 (2013).
26. Abel, J. *et al.* AI powered quantification of nuclear morphology in cancers enables prediction of genome instability and prognosis. *NPJ Precis Oncol* **8**, 134 (2024).
27. Wu, Z. *et al.* Reduced expression of lamin A/C correlates with poor histological differentiation and prognosis in primary gastric carcinoma. *Journal of Experimental & Clinical Cancer Research* **28**, 8 (2009).
28. Matsumoto, A. *et al.* Global loss of a nuclear lamina component, lamin A/C, and <scp>LINC</scp> complex components <scp>SUN</scp> 1, <scp>SUN</scp> 2, and nesprin-2 in breast cancer. *Cancer Med* **4**, 1547–1557 (2015).
29. Gong, G. *et al.* Loss of lamin A but not lamin C expression in epithelial ovarian cancer cells is associated with metastasis and poor prognosis. *Pathol Res Pract* **211**, 175–182 (2015).
30. Belt, E. J. Th. *et al.* Loss of lamin A/C expression in stage II and III colon cancer is associated with disease recurrence. *Eur J Cancer* **47**, 1837–1845 (2011).
31. Bell, E. S. & Lammerding, J. Causes and consequences of nuclear envelope alterations in tumour progression. *Eur J Cell Biol* **95**, 449–464 (2016).
32. Zasadil, L. M. *et al.* Cytotoxicity of Paclitaxel in Breast Cancer Is due to Chromosome Missegregation on Multipolar Spindles. *Sci Transl Med* **6**, (2014).
33. Oberhofer, A. *et al.* Molecular underpinnings of cytoskeletal cross-talk. *Proceedings of the National Academy of Sciences* **117**, 3944–3952 (2020).
34. Pradeau-Phélut, L. & Etienne-Manneville, S. Cytoskeletal crosstalk: A focus on intermediate filaments. *Curr Opin Cell Biol* **87**, 102325 (2024).
35. Prahlad, V., Yoon, M., Moir, R. D., Vale, R. D. & Goldman, R. D. Rapid Movements of Vimentin on Microtubule Tracks: Kinesin-dependent Assembly of Intermediate Filament Networks. *J Cell Biol* **143**, 159–170 (1998).
36. Gurland, G. & Gundersen, G. G. Stable, detyrosinated microtubules function to localize vimentin intermediate filaments in fibroblasts. *J Cell Biol* **131**, 1275–1290 (1995).
37. Janssen, A. F. J., Breusegem, S. Y. & Larrieu, D. Current Methods and Pipelines for Image-Based Quantitation of Nuclear Shape and Nuclear Envelope Abnormalities. *Cells* **11**, 347 (2022).
38. Broers, J. L. V. *et al.* Decreased mechanical stiffness in LMNA−/− cells is caused by defective nucleo-cytoskeletal integrity: implications for the development of laminopathies. *Hum Mol Genet* **13**, 2567–2580 (2004).
39. Cain, N. E. & Starr, D. A. SUN proteins and nuclear envelope spacing. *Nucleus* **6**, 2–7 (2015).

40. Barad, B. A., Medina, M., Fuentes, D., Wiseman, R. L. & Grotjahn, D. A. Quantifying organellar ultrastructure in cryo-electron tomography using a surface morphometrics pipeline. *Journal of Cell Biology* **222**, (2023).
41. Kochin, V. *et al.* Interphase phosphorylation of lamin A. *J Cell Sci* **127**, 2683–2696 (2014).
42. Bertacchini, J. *et al.* The protein kinase Akt/PKB regulates both prelamin A degradation and Lmna gene expression. *FASEB Journal* **27**, 2145–2155 (2013).
43. Okano, J. I. & Rustgi, A. K. Paclitaxel Induces Prolonged Activation of the Ras/MEK/ERK Pathway Independently of Activating the Programmed Cell Death Machinery. *Journal of Biological Chemistry* **276**, 19555–19564 (2001).
44. Lu, P. H. *et al.* Paclitaxel induces apoptosis through activation of nuclear protein kinase C-δ and subsequent activation of Golgi associated Cdk1 in human hormone refractory prostate cancer. *Journal of Urology* **186**, 2434–2441 (2011).
45. Li, Q. *et al.* A Syntaxin 1, $G\alpha_o$, and N-Type Calcium Channel Complex at a Presynaptic Nerve Terminal: Analysis by Quantitative Immunocolocalization. *The Journal of Neuroscience* **24**, 4070–4081 (2004).
46. Yamori, T., Sato, S., Chikazawa, H. & Kadota, T. Anti-tumor Efficacy of Paclitaxel against Human Lung Cancer Xenografts. *Japanese Journal of Cancer Research* **88**, 1205–1210 (1997).
47. Milas, L. *et al.* Kinetics of mitotic arrest and apoptosis in murine mammary and ovarian tumors treated with taxol. *Cancer Chemother Pharmacol* **35**, 297–303 (1995).
48. Fuchs, D. A. & Johnson, R. K. Cytologic evidence that taxol, an antineoplastic agent from Taxus brevifolia, acts as a mitotic spindle poison. *Cancer Treat Rep* **62**, 1219–22 (1978).
49. Kay, K., Dolcy, K., Bies, R. & Shah, D. K. Estimation of Solid Tumor Doubling Times from Progression-Free Survival Plots Using a Novel Statistical Approach. *AAPS J* **21**, 27 (2019).
50. Denduluri, N. *et al.* Phase II Trial of Ixabepilone, an Epothilone B Analog, in Patients With Metastatic Breast Cancer Previously Untreated With Taxanes. *Journal of Clinical Oncology* **25**, 3421–3427 (2007).
51. Lopez-Soler, R. I., Moir, R. D., Spann, T. P., Stick, R. & Goldman, R. D. A role for nuclear lamins in nuclear envelope assembly. *J Cell Biol* **154**, 61–70 (2001).
52. Gerace, L. & Burke, B. Functional Organization of the Nuclear Envelope. *Annu Rev Cell Biol* **4**, 335–374 (1988).
53. Usman, S. *et al.* Vimentin Is at the Heart of Epithelial Mesenchymal Transition (EMT) Mediated Metastasis. *Cancers (Basel)* **13**, 4985 (2021).
54. Satelli, A. & Li, S. Vimentin in cancer and its potential as a molecular target for cancer therapy. *Cellular and Molecular Life Sciences* **68**, 3033–3046 (2011).
55. Gonçalves, J. C., Quintremil, S., Yi, J. & Vallee, R. B. Nesprin-2 Recruitment of BicD2 to the Nuclear Envelope Controls Dynein/Kinesin-Mediated Neuronal Migration In Vivo. *Current Biology* **30**, 3116-3129.e4 (2020).
56. Wilson, M. H. & Holzbaur, E. L. F. Nesprins anchor kinesin-1 motors to the nucleus to drive nuclear distribution in muscle cells. *Development* **142**, 218–228 (2015).

57. Wilhelmsen, K. *et al.* Nesprin-3, a novel outer nuclear membrane protein, associates with the cytoskeletal linker protein plectin. *J Cell Biol* **171**, 799–810 (2005).
58. Pan, K.-W. & Chen, H.-C. Perinuclear assembly of vimentin intermediate filaments induces cancer cell nuclear dysmorphia. *Journal of Biological Chemistry* **300**, 107981 (2024).
59. Gerlitz, G., Reiner, O. & Bustin, M. Microtubule dynamics alter the interphase nucleus. *Cellular and Molecular Life Sciences* **70**, 1255–1268 (2013).
60. Crisp, M. *et al.* Coupling of the nucleus and cytoplasm: Role of the LINC complex. *J Cell Biol* **172**, 41–53 (2006).
61. Swift, J. *et al.* Nuclear Lamin-A Scales with Tissue Stiffness and Enhances Matrix-Directed Differentiation. *Science (1979)* **341**, (2013).
62. Cho, S., Irianto, J. & Discher, D. E. Mechanosensing by the nucleus: From pathways to scaling relationships. *Journal of Cell Biology* **216**, 305–315 (2017).
63. Karoutas, A. *et al.* The NSL complex maintains nuclear architecture stability via lamin A/C acetylation. *Nat Cell Biol* **21**, 1248–1260 (2019).
64. Blank, M. Targeted Regulation of Nuclear Lamins by Ubiquitin and Ubiquitin-Like Modifiers. *Cells* **9**, 1340 (2020).
65. Donnaloja, F., Carnevali, F., Jacchetti, E. & Raimondi, M. T. Lamin A/C Mechanotransduction in Laminopathies. *Cells* **9**, 1306 (2020).
66. Sosa, B. A., Rothballer, A., Kutay, U. & Schwartz, T. U. LINC Complexes Form by Binding of Three KASH Peptides to Domain Interfaces of Trimeric SUN Proteins. *Cell* **149**, 1035–1047 (2012).
67. Gilbert, H. T. J. *et al.* Nuclear decoupling is part of a rapid protein-level cellular response to high-intensity mechanical loading. *Nat Commun* **10**, 4149 (2019).
68. Krshnan, L. *et al.* Regulated degradation of the inner nuclear membrane protein SUN2 maintains nuclear envelope architecture and function. *Elife* **11**, (2022).
69. Raab, M. *et al.* ESCRT III repairs nuclear envelope ruptures during cell migration to limit DNA damage and cell death. *Science (1979)* **352**, 359–362 (2016).
70. Vargas, J. D., Hatch, E. M., Anderson, D. J. & Hetzer, M. W. Transient nuclear envelope rupturing during interphase in human cancer cells. *Nucleus* **3**, 88–100 (2012).
71. De Vos, W. H. *et al.* Repetitive disruptions of the nuclear envelope invoke temporary loss of cellular compartmentalization in laminopathies. *Hum Mol Genet* **20**, 4175–4186 (2011).
72. Wagner, F. R. *et al.* Preparing samples from whole cells using focused-ion-beam milling for cryo-electron tomography. *Nat Protoc* **15**, 2041–2070 (2020).
73. Zuiderveld, K. Contrast limited adaptive histogram equalization. in *Graphics gems IV* 474–485 (Academic Press Professional, Inc., 1994).
74. Lowe, D. G. Distinctive Image Features from Scale-Invariant Keypoints. *Int J Comput Vis* **60**, 91–110 (2004).
75. Mastronarde, D. N. Automated electron microscope tomography using robust prediction of specimen movements. *J Struct Biol* **152**, 36–51 (2005).
76. Eisenstein, F. *et al.* Parallel cryo electron tomography on in situ lamellae. *Nat Methods* **20**, 131–138 (2023).
77. Tegunov, D. & Cramer, P. Real-time cryo-electron microscopy data preprocessing with Warp. *Nat Methods* **16**, 1146–1152 (2019).

78. Zheng, S. *et al.* AreTomo: An integrated software package for automated marker-free, motion-corrected cryo-electron tomographic alignment and reconstruction. *J Struct Biol X* **6**, 100068 (2022).
79. Kremer, J. R., Mastronarde, D. N. & McIntosh, J. R. Computer Visualization of Three-Dimensional Image Data Using IMOD. *J Struct Biol* **116**, 71–76 (1996).

Supplementary Material

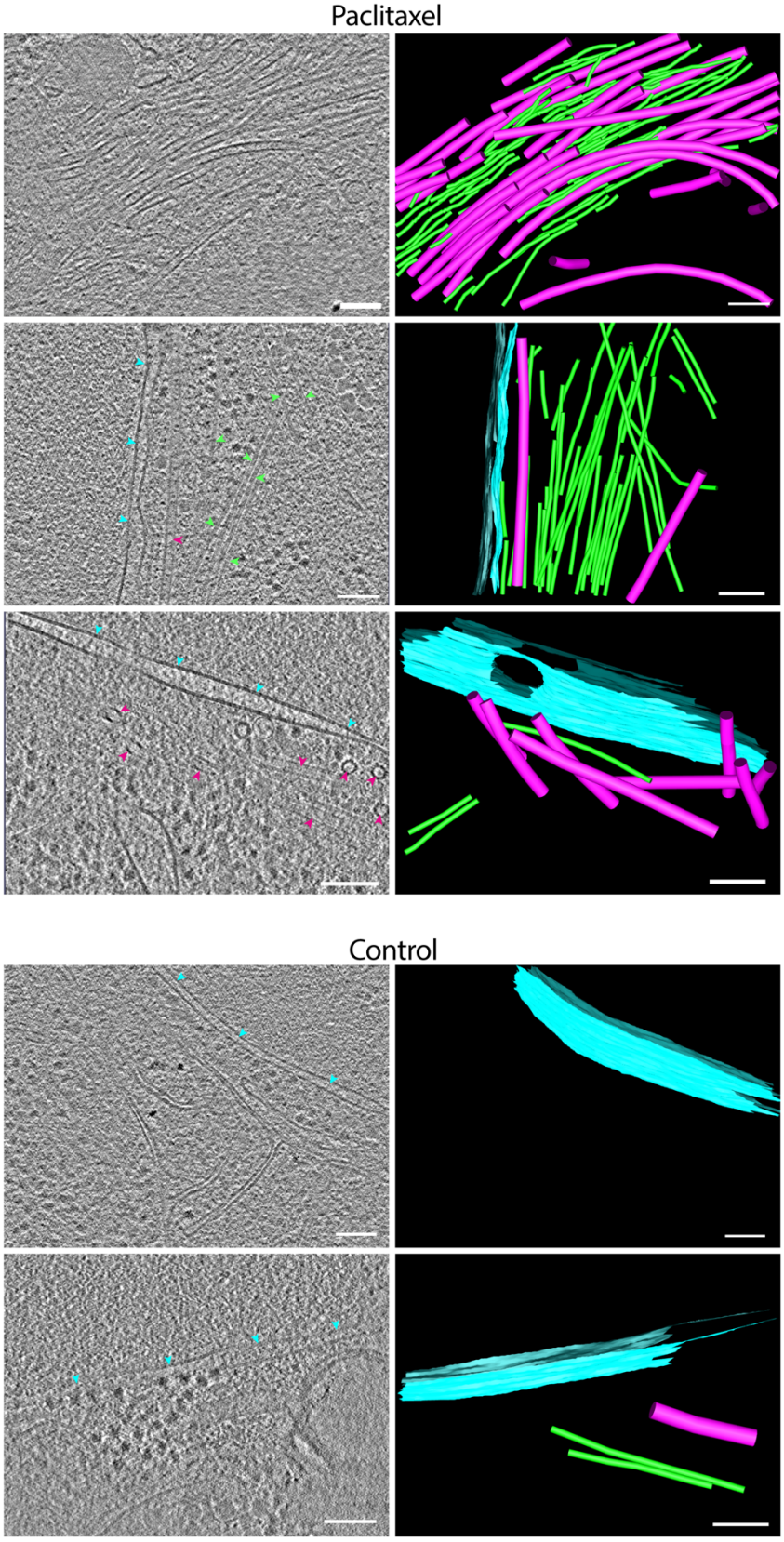

Supplementary Figure 1 – Paclitaxel induces bundling of microtubules and vimentin filaments adjacent to the NE. Left panels shows 2D slices of reconstructed tomograms from paclitaxel-treated or control cells. Right panels show segmentations from these tomograms of microtubules (magenta), vimentin filaments (green), and the NE (cyan), which are marked with arrowheads of the same colour in the tomogram slice. Scale bars = 100 nm.

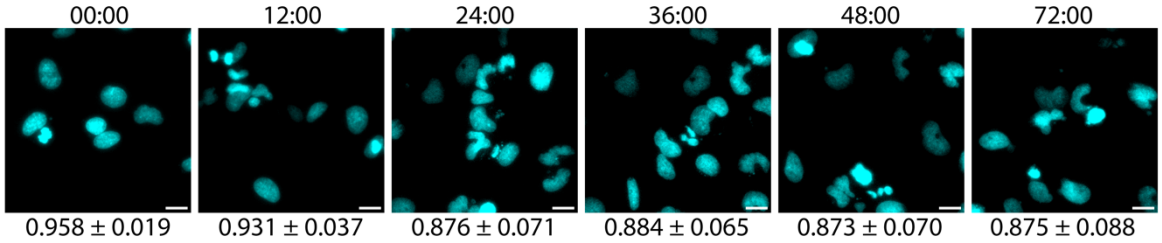

Supplementary Figure 2 – Paclitaxel induces nuclear deformation. Example of images used for nuclear solidity quantification in Figure 2A. Frames from a live-cell movie of Hoechst-stained nuclei 0-72 h after addition of 5 nM paclitaxel are shown, together with the mean nuclear solidity measurements ± the standard deviation from these images.

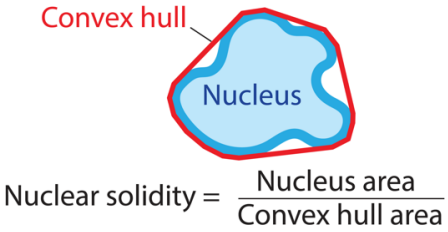

Supplementary Figure 3 - Nuclear solidity to quantify nuclear deformation. Nuclear solidity is defined as the nucleus area (blue) divided by the convex hull area of the nucleus[37] (red).

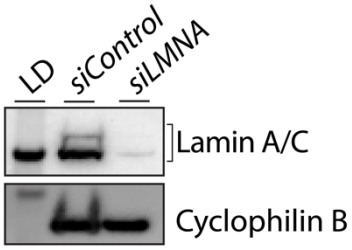

Supplementary Figure 4 - Lamin A/C knockdown. Western Blot confirming knockdown of Lamin A and Lamin C following transfection with siRNA against *LMNA* (siLMNA), compared to with control siRNA (siControl). Cyclophilin B was used as the loading control. Lane 1 shows protein ladder (LD; 62 kDa for Lamin A/C panel, and 28 kDa for Cyclophilin B panel).

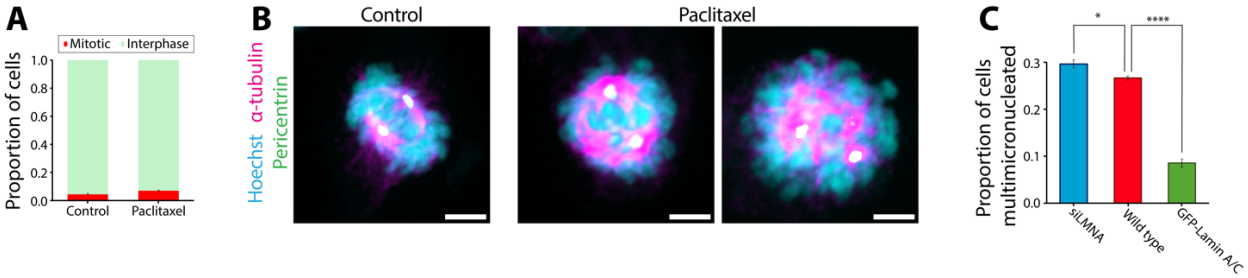

Supplementary Figure 5 - Paclitaxel results in multimicronucleation following exit from aberrant mitosis. (A) Bar graph showing the proportion of cells that were in interphase (green) versus mitosis (red) following 30 h incubation in 5 nM paclitaxel or control media. Mitotic cells were identified by the presence of condensed chromosomes and a mitotic spindle following staining for DNA using Hoechst and microtubules using α-tubulin

immunofluorescence. Error bars represent the standard deviation from three biological repeats. **(B)** Confocal micrographs of cells fixed after 24 h incubation in control media or 5 nM paclitaxel. Cells were stained for DNA using Hoechst (cyan), microtubules using α-tubulin immunofluorescence (magenta), and centrosomes using pericentrin immunofluorescence (green). Scale bars = 5 µm. **(C)** Bar graph comparing the proportion of wild-type (red), Lamin A/C knockdown (siLMNA – blue), and GFP-Lamin A/C overexpressing (green) cells that were multimicronucleated following 24 h incubation in 5 nM paclitaxel. Multimicronucleated cells were identified from confocal micrographs of cells stained for DNA using Hoechst. Statistical analysis: t-test versus wild type. siLMNA: P=0.0346 (*); GFP-Lamin A/C: P=4.86 x 10^{-5} (****).

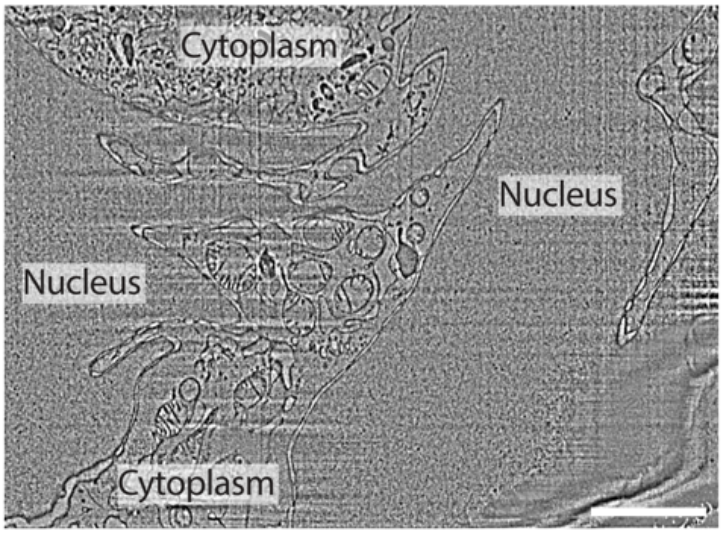

Supplementary Figure 6 - Paclitaxel results in NE deformation. Single slice from FIB-SEM volume imaging of a paclitaxel-treated cell showing severe NE invaginations and blebs. Scale bar = 2 µm.

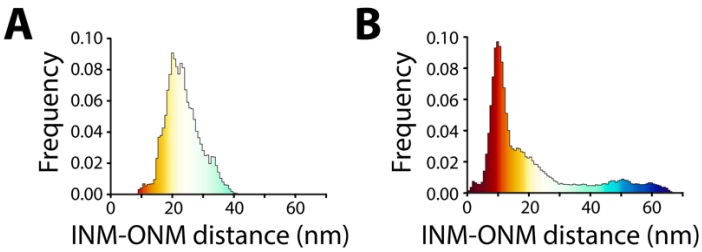

Supplementary Figure 7 – Paclitaxel alters nuclear membrane spacing. Histograms showing the ONM-INM distance from **(A)** the control tomogram, and **(B)** the paclitaxel tomogram in Figure 2F.

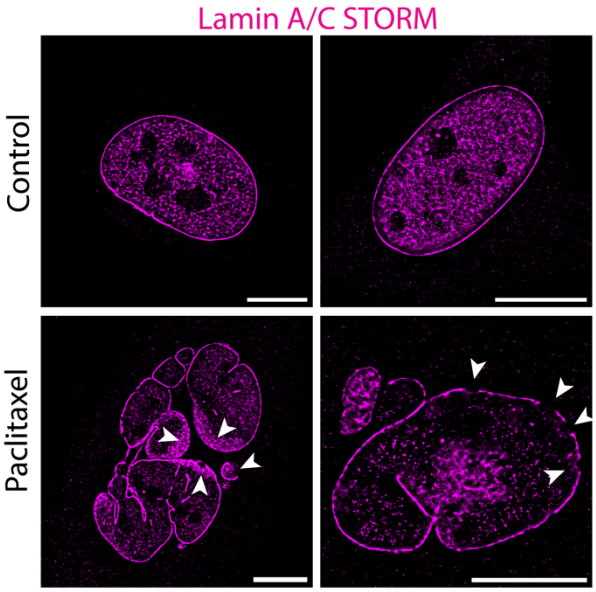

Supplementary Figure 8 – Paclitaxel results in a patchy nuclear lamina. STORM images of cells fixed after 16 h incubation in control media or 5 nM paclitaxel. Lamin A/C was stained using immunofluorescence (magenta). Scale bars = 10 µm. Holes in the nuclear lamina are marked with arrowheads.

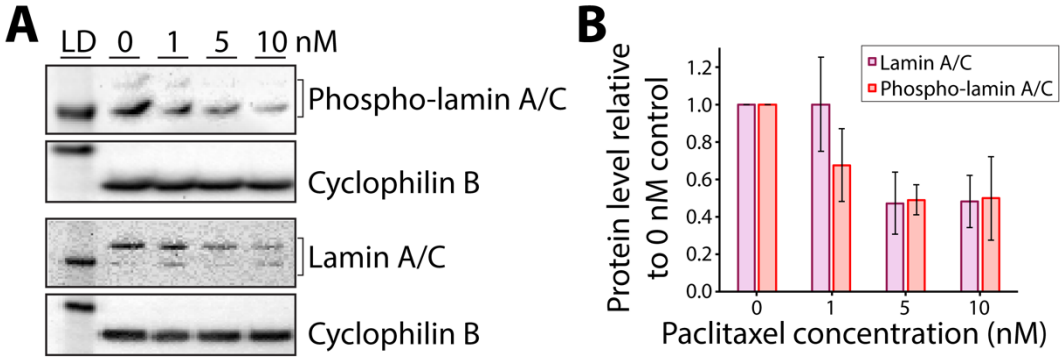

Supplementary Figure 9 – Paclitaxel does not affect Lamin A/C interphase phosphorylation. (A) Western blots for Lamin A/C and phospho-Ser404 Lamin A/C of whole cell lysates following 16 h incubation in media containing 0, 1, 5, or 10 nM paclitaxel. Cyclophilin B was used as a loading control. Lane 1 shows protein ladder (LD; 62 kDa for [Phospho]Lamin A/C panels, and 28 kDa for Cyclophilin B panels). **(B)** Quantification of Lamin A/C and phospho-Lamin A/C levels from (A). Each band was normalised to the corresponding Cyclophilin B loading control. Error bars represent the standard deviation from three biological repeats.

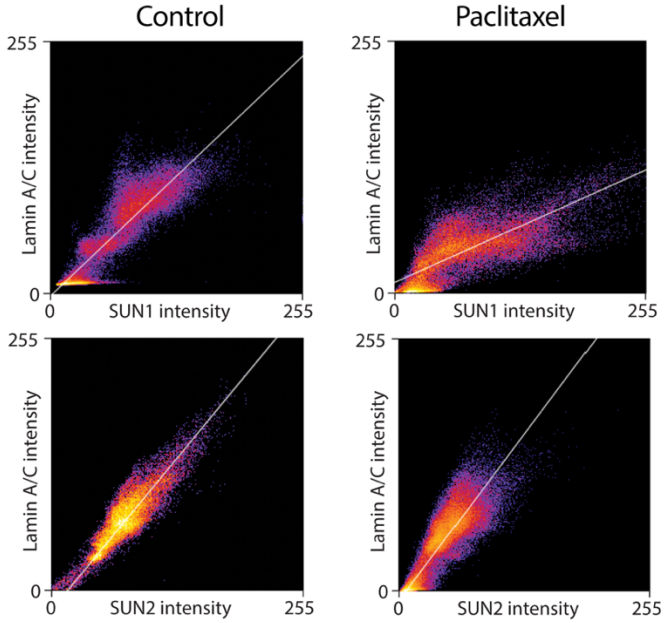

Supplementary Figure 10 – Colocalisation between Lamin A/C and SUN1 or SUN2. Scatterplots of Lamin A/C fluorescence intensity versus SUN1/SUN2 fluorescence intensity for each pixel of images in Figure 3D.

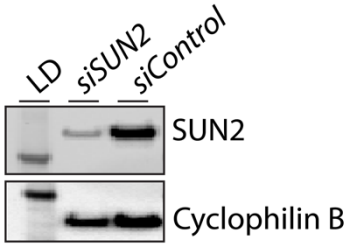

Supplementary Figure 11 – SUN2 knockdown. Western Blot confirming knockdown of SUN2 following transfection with siRNA against *SUN2* (siSUN2), compared to with control siRNA (siControl). Cyclophilin B was used as the loading control. Lane 1 shows protein ladder (LD; 62 kDa for SUN2 panel, and 28 kDa for Cyclophilin B panel).

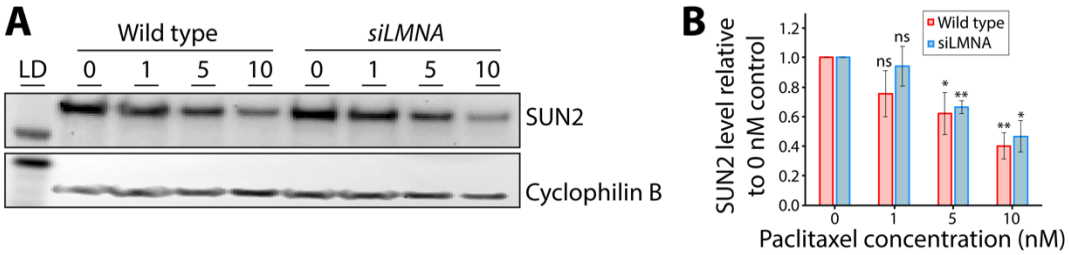

Supplementary Figure 12 – The paclitaxel-induced decreased in SUN2 levels occurs independently of Lamin A/C. (A) Western blots for SUN2 of whole cell lysates from wild-type or Lamin A/C knockdown (siLMNA) cells following 16 h incubation in media containing 0, 1, 5, or 10 nM paclitaxel. Cyclophilin B was used as a loading control. Lane 1 shows protein ladder (LD; 62 kDa for SUN2 panel, and 28 kDa for Cyclophilin B panel). **(B)** Quantification of SUN2 levels from (A). Each band was normalised to the corresponding Cyclophilin B loading control. Error bars represent the standard deviation from three biological repeats. Statistical analysis: one sample t-test with null hypothesis mean = 1. Wild type: 1 nM P=0.1112; 5 nM P=0.0445; 10 nM P=0.0070. siLMNA: 1 nM P=0.5221; 5 nM P=0.0053; 10 nM P=0.0132. Ns = non-significant = P>0.05; * P<0.05; ** P<0.01.

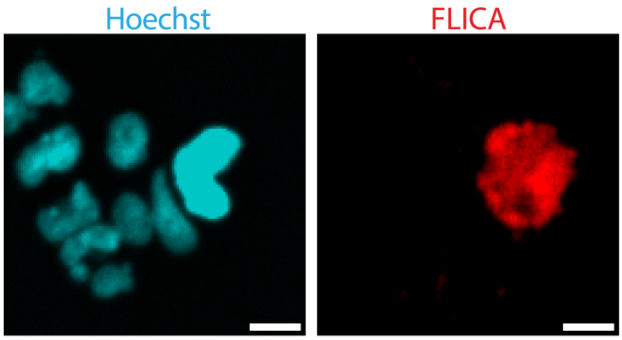

Supplementary Figure 13 – Cell viability analysis. Example micrograph of cells stained for DNA with Hoechst (cyan), and active caspases using FLICA (red). Scale bars = 10 µm.

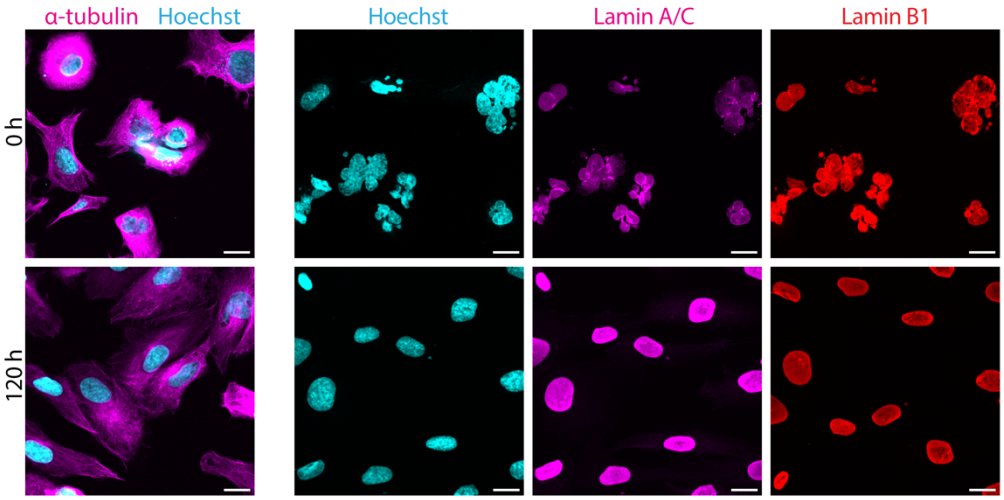

Supplementary Figure 14 – The microtubule organisation and nuclear lamina recover following paclitaxel removal. Confocal micrographs of cells fixed 0 or 120 h after removal of 5 nM paclitaxel. Cells were stained for DNA using Hoechst (cyan), and microtubules using α-tubulin immunofluorescence (magenta); or for DNA using Hoechst (cyan), and Lamin A/C (magenta) and Lamin B1 (red) using immunofluorescence. Scale bars = 20 µm.

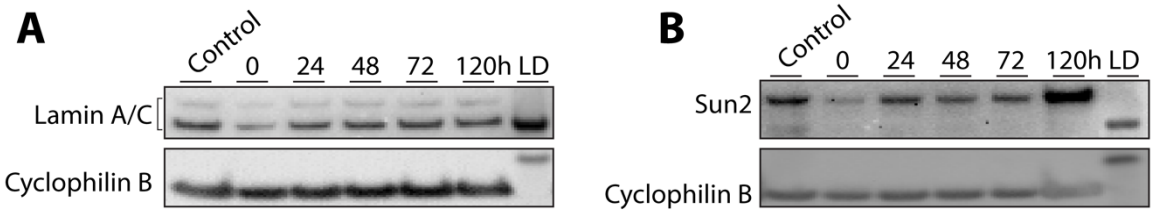

Supplementary Figure 15 – Lamin A/C and SUN2 protein levels recover following paclitaxel removal. Western blots for Lamin A/C **(A)** and SUN2 **(B)** of whole cell lysates after 0, 24, 48, 72, or 120 h following removal of 5 nM paclitaxel. Lane 1 contains untreated cell control. Cyclophilin B was used as a loading control. Lane 7 shows protein ladder (LD; 62 kDa for Lamin A/C and SUN2 panels, and 28 kDa for Cyclophilin B panels).

siRNA	Target mRNA	Source
siLMNA	*LMNA*	Ambion 4392420 Assay ID s530951
siSUN2	*SUN2*	Ambion 4392420 Assay ID s24467
siControl	N/A	Ambion 4390844

Supplementary Table 1 – Details of siRNAs used for knockdowns.

Antibody	Dilution (IF – immunofluorescence; WB – Western blot)	Source
Mouse anti-α tubulin	IF: 1:100	Invitrogen A11126
Rabbit anti-vimentin	IF: 1:200	Abcam ab92547
Rabbit anti-Lamin B1	IF: 1:200; WB: 1:2,000	Abcam ab16048
Mouse anti-Lamin A/C	IF: 1:200; WB: 1:1,000	Santa Cruz sc7292
Mouse anti-phospho-Ser404 Lamin A/C	WB: 1:1,000	Sigma ABT1387
Rabbit anti-SUN1	IF: 1:200; WB: 1:2,000	Sigma HPA008346
Rabbit anti-SUN2	IF: 1:500; WB: 1:2,000	Abcam ab124916
Rabbit anti-Cyclophilin B	WB: 1:2,000	Abcam ab16045
Donkey anti-Mouse IgG – Alexa 555	IF: 1:500	Abcam ab150110
Donkey anti-Mouse IgG – Alexa 647	IF: 1:500	Abcam ab150111
Donkey anti-Rabbit IgG – Alexa 555	IF: 1:500	Abcam ab150074
Donkey anti-Rabbit IgG – Alexa 647	IF: 1:500	Abcam ab181347
Goat anti-Rabbit IgG - HRP	WB: 1:15,000	Abcam ab6721
Goat anti-Mouse IgG - HRP	WB: 1:10,000	Abcam ab97023

Supplementary Table 2 – Details of antibodies used for immunofluorescence and Western blotting.